Title

Efficient Front-Rear Coupling in Neutrophil Chemotaxis by Dynamic Myosin II Localization.

Journal

Developmental Cell, 49(2)

Authors

Chan, Caleb
Hadjitheodorou, Amalia
Lam, Pui-Ying
et al.

Publication Date

2019-04-22

DOI

10.1016/j.devcel.2019.03.025

Peer reviewed

HHS Public Access

Author manuscript

Dev Cell. Author manuscript; available in PMC 2019 August 24.

Published in final edited form as:

Dev Cell. 2019 April 22; 49(2): 189–205.e6. doi:10.1016/j.devcel.2019.03.025.

Efficient Front-Rear Coupling in Neutrophil Chemotaxis by Dynamic Myosin II Localization

Tony Y.-C. Tsai[1,2,4,a], **Sean R. Collins**[1,b], **Caleb K. Chan**[2,4], **Amalia Hadjitheodorou**[2,3,4], **Pui-ying Lam**[5,6,c], **Sunny S. Lou**[1,2,4], **Hee Won Yang**[1], **Julianne Jorgensen**[7], **Felix Ellett**[7], **Daniel Irimia**[7], **Michael W. Davidson**[8,†], **Robert S. Fischer**[9], **Anna Huttenlocher**[5], **Tobias Meyer**[1], **James E. Ferrell Jr.**[1,2], **Julie A. Theriot**[2,4,d,*]

[1]Department of Chemical and Systems Biology, Stanford University School of Medicine, Stanford CA 94305

[2]Department of Biochemistry, Stanford University School of Medicine, Stanford CA 94305

[3]Department of Bioengineering, Stanford University School of Medicine, Stanford CA 94305

[4]Howard Hughes Medical Institute, Stanford University School of Medicine, Stanford CA 94305

[5]Department of Pediatrics and Medical Microbiology and Immunology, University of Wisconsin-Madison, Madison, WI 53706

[6]Program in Cellular and Molecular Biology, University of Wisconsin-Madison, Madison, WI 53706

[7]Department of Surgery, BioMEMS Resource Center, Massachusetts General Hospital, Harvard Medical School, Boston, MA 02129

[8]National High Magnetic Field Laboratory, Department of Biological Science, The Florida State University, Tallahassee, FL 32304

[9]National Heart, Lung and Blood Institute, National Institutes of Health, Bethesda, Maryland 20892

SUMMARY

Efficient chemotaxis requires rapid coordination between different parts of the cell in response to changing directional cues. Here we investigate the mechanism of front-rear coordination in chemotactic neutrophils. We find that changes in the protrusion rate at the cell front are instantaneously coupled to changes in retraction at the cell rear, while myosin II accumulation at

jtheriot@uw.edu, phone 1-206-543-3397.

AUTHOR CONTRIBUTIONS

T.Y-C.T., J.E.F., J.A.T. designed the majority of the experiments. T.Y-C.T., S.R.C., C.K.C., A.Ha., P.-Y.L, S.S.L, H.W.Y. performed the experiments. S.R.C., H.W.Y., and T.M. designed the RhoA sensor experiments, J.J., F.E. and D.I. designed the microfluidic device, P.-Y.L, R.S.F. and A.Hu. designed the zebrafish experiments, T.Y-C.T., C.K.C and A.Ha. analyzed the data. M.W. D. provided reagents, T.Y-C.T. and J.A.T. wrote the manuscript with assistance from all authors.

[a]Current address: Department of Systems Biology, Harvard Medical School, Boston, MA 02115

[b]Current address: Department of Microbiology and Molecular Genetics, University of California, Davis, Davis, CA 95616

[c]Current address: Department of Pharmacology and Toxicology, College of Pharmacy, University of Utah, Salt Lake City, UT 84112

[d]Current address: Department of Biology, University of Washington, Seattle, WA 98195

[†]Deceased

[*]Lead Contact

DECLARATION OF INTERESTS

The authors declare no competing interests.

the rear exhibits a reproducible 9-15 sec lag. In turning cells, myosin II exhibits dynamic side-to-side relocalization at the cell rear in response to turning of the leading edge, and facilitates efficient turning by rapidly re-orienting the rear. These manifestations of front-rear coupling can be explained by a simple quantitative model incorporating reversible actin-myosin interactions with a rearward-flowing actin network. Finally, the system can be tuned by the degree of myosin regulatory light chain (MRLC) phosphorylation, which appears to be set in an optimal range to balance persistence of movement and turning ability.

INTRODUCTION

The neutrophil is one of the fastest migrating cells in the human body. Upon exposure to a gradient of chemoattractant, neutrophils navigate efficiently through interstitial spaces toward sites of inflammation to perform their immune function by phagocytosing and killing bacteria and fungi (Segal, 2005). Substantial progress has been made toward understanding neutrophil chemotaxis at the level of signaling (Wang, 2009). Binding of the chemoattractant to its cognate G-protein-coupled receptor activates signal transduction cascades that diverge into a “front” module and a “back” module. At the front, activation of $G_{\alpha i}$ and $G_{\beta\gamma}$ initiates an activating cascade, including the phosphoinositide 3-kinase (PI(3)K) and small GTPases Rac and Cdc42, leading to an increase in actin polymerization (Wang et al., 2002). At the back of the cell, $G_{\alpha 12/13}$ activates the GTPase RhoA, which in turn activates the kinase ROCK1, leading to an increase in the phosphorylation of myosin regulatory light chain (MRLC) and enhanced myosin contractility (Xu et al., 2003). RhoA has been shown to have relatively higher activity at the rear of migrating neutrophil-like cells (Wong et al., 2006; Yang et al., 2015) and also to reinforce overall cell polarity at the rear (Wong et al., 2007; Xu et al., 2003). Both the front and back modules have positive feedback loops for self-amplification and stabilization of polarity (Hind et al., 2016; Wang et al., 2002; Weiner et al., 2002). The spatial domains of the two modules are mutually exclusive within an individual cell, allowing for spontaneous symmetry breaking and the robust development of front-rear polarity (Xu et al., 2003).

In addition, plasma membrane tension has been shown to act as a long-range inhibitor to mechanically coordinate neutrophil cell polarity. Specifically, membrane tension rises as a new protrusion initiates, and this global negative feedback prevent other parts of the cell from developing a second protrusion (Houk et al., 2012). However, there is also evidence that there must be positive reinforcement between the front and the back modules, as well as mutual inhibition, as the structural signatures of the cell rear such as myosin II accumulation and phosphorylation of the myosin regulatory light chain are not weakest in cells with strong leading edges (Wang et al., 2013).

Recently, several lines of evidence have suggested that cytoskeleton-based transport via retrograde actin flow in the cell frame of reference may play an important role in the global coordination of migrating cells. Across many motile cell types, faster actin network flow is correlated with increased cell directional persistence and increased cell speed (Maiuri et al., 2015), a general finding consistent with the hypothesis that some regulatory factors that directly bind to the actin network and are transported by its flow are able to reinforce cell

polarity at the rear. One particularly attractive candidate for such a regulatory factor is myosin II, which forms filaments that bind to the actin network and are transported across the entire cell length in many motile cell types including fish epidermal keratocytes (Svitkina et al., 1997; Wilson et al., 2010), mouse dendritic cells (Maiuri et al., 2015), zebrafish germ layer progenitors (Ruprecht et al., 2015), and even confined HeLa cells (Liu et al., 2015). At the cell rear, myosin II activity is thought to contribute to cell rear retraction through its contractile activity and/or its ability to disassemble the actin network (Reymann et al., 2012; Wilson et al., 2010).

In this work, we have investigated the temporal relationships among leading edge protrusion, rear retraction, and rear localization of myosin II in neutrophils. Neutrophils exhibit rapid changes of migration speed and direction (Senda et al., 1975), enabling a definitive comparison of the relative timing of these events in cell migration. We have identified a stereotypical front-rear coupling pattern where membrane retraction at the cell rear is instantaneously coupled to changes at the front but with myosin accumulation lagging by about 9-15 sec. Local RhoA activities do not appear to be a direct trigger for myosin II accumulation; rather the kinetics we observe are most compatible with a model where tension in the plasma membrane provides near-instantaneous coupling between protrusion at the cell front and retraction at the rear, compressing the actin network at the rear and consequently leading to myosin II-driven network contraction and disassembly. In a turning cell, myosin II accumulation appears to contribute to the rapid reorientation of the cell rear in response to changes of protrusion direction at the front. We propose that the timing and spatial characteristics of the quick (9-15 sec) response observed at the cell rear are mediated by myosin retrograde flow, membrane tension, and the intrinsic accumulation and disassembly dynamics of contracting myosin working together to coordinate the machinery of movement across the entire cell.

RESULTS

Protrusion and retraction are tightly coupled in migrating HL60 Cells

We generated a neutrophil-like HL60 cell line stably expressing both actin-YFP and myosin regulatory light chain-mApple (named MRLC-mApple hereafter), and observed actin and myosin dynamics during HL60 cell migration in a uniform concentration of the chemoattractant fMLP. We confined the cells underneath an agarose pad (Figures S1A and S1B), an environment more similar to the confined spaces through which a neutrophil migrates *in vivo* than an open coverslip, and which promotes active directional migration for a variety of cell types (Liu et al., 2015). We obtained the instantaneous protrusion and retraction speeds by calculating the area of the newly-protruded and newly-retracted regions (Figure 1A and Movie S1), and noticed a strong correlation between changes in the rate of protrusion at the front and the rate of retraction at the rear with no detectable temporal offset (Figure 1B). Consequently, the average projected area of each cell remained remarkably constant over periods of many minutes (Figure 1B).

We next examined the localization of myosin II, using MRLC-mApple as a proxy, relative to the change of protrusion and retraction speeds. MRLC accumulation is often observed at the back of the cell, but at the front of the uropod. We defined a metric, the myosin rearward

localization score (hereafter MRS), to calculate the weighted average of myosin intensity from the front to the back of the cell (see Methods, Figures S1C and S1D, and Movie S1). The score is zero when myosin is symmetric along the front-rear axis, and greater if myosin is more localized to the rear. We compared the MRS with the protrusion speed over time for individual cells (Figure 1B). Cross-correlation analysis revealed that the most significant positive correlation between the two required a 9 second temporal offset for the example shown (Figure 1C and 1D); that is, an increase of protrusion speed at a given time correlated with a more rear-localized myosin distribution 9 seconds later (Figure 1D). This observation that protrusion speed and retraction speed are closely synchronized, whereas myosin localization lags behind by about 9-15 sec, was highly reproducible across a population of HL60 cells (Figures 1E and 1F; Figure S1E).

In addition, we examined the temporal coupling between retraction at the cell rear and local activation of the small GTPase RhoA using a FRET-based reporter (Yang et al., 2015). In contrast to the strong and reproducible temporal coupling between cell protrusion and myosin II rearward localization as described above, we could not detect any statistically significant coupling between the rearward enrichment of RhoA activity and the speed of cell protrusion (Figure S1F). The lack of coupling suggests that RhoA is not the direct mediator between the change of protrusion speed and the response of myosin, but rather plays a permissive role for rear polarity. Note that RhoC remains a possible mediator of myosin response, although its transcript level is 10 times less abundant than RhoA (data not shown).

Myosin II activity has previously been shown to be important for maintenance of polarity of neutrophils *in vivo* (Yoo et al., 2010) and for directed migration in neutrophil-like cells (Wong et al., 2007). Our observation that myosin accumulates only after the initiation of rear retraction suggests that myosin at the cell rear is contributing to motility in some other way than simply driving retraction, and membrane tension could be the primary mediator of the coupling between protrusion and retraction (Houk et al., 2012).

Myosin retrograde flow and membrane retraction facilitate the rapid protrusion-myosin coupling

To understand how changes in protrusion dynamics could affect myosin localization over the observed characteristic 9-15 sec time scale, we examined the actin-myosin interaction by imaging actin-YFP and MRLC-mApple simultaneously using total internal reflection fluorescence microscopy (TIRF) (Figures 2A and 2B, Movie S2). Both actin and myosin II formed sub-micron scale puncta that are likely to be regions within the F-actin meshwork with relatively high local actin density, and concomitant locally high concentrations of myosin II filaments that bind to the actin network (Figures 2A-2C). In the laboratory frame of reference, the actin and myosin II puncta appeared to be essentially static relative to the coverslip substrate until they were brought forward by the large contracting myosin clusters at the rear (Figures 2C and 2D, Movie S2). That is, in the cell frame of reference, both the actin and myosin II puncta moved toward the rear of the cell, and the speed of this retrograde flow was equal to the speed of the cell in the laboratory frame of reference (Figure 2E and Movie S2). The fluorescence intensity of the actin puncta started decreasing in the region of the cell where myosin II puncta first appeared (Figures 2C-2E), and the

myosin II puncta steadily increased in intensity while moving towards the rear of the cell (in the cell frame of reference), with a characteristic doubling time on the order of 40 sec (Figures 2F and 2G). The apparent stability of the accumulating myosin II puncta enabled us to track many of the individual puncta from their initial sites of assembly near the actin-rich leading edge all the way to the rear of the cell where they were incorporated into the very dense focal accumulations that are characteristic of rapidly moving cells with a high MRS. Thus, we observe that the overall enrichment of myosin II at the rear of the cell is due to a combination of rearward transport of existing puncta and further accumulation driven by association of myosin II filaments binding to the flowing actin network from a cytoplasmic pool.

From first principles, the time-scale for the rearward accumulation of myosin II should depend on the stability of the association of myosin with the actin network, the diffusion coefficient of free myosin, and the rates of actin network retrograde flow and membrane crushing of the network at the rear (Figure 2H). In a simple mathematical model taking all of these factors into account, we can measure most of the critical rates experimentally, and estimate the others (see Methods, Figures 2H and S2). This simple framework is sufficient to robustly reproduce the characteristic 9-15 sec response of myosin accumulation at the cell rear to changes in protrusion at the cell front over a wide range (~50X) of reasonable parameters (Figures 2I-2K). This suggests that simple interactions among actin, myosin, and the cell plasma membrane are sufficient to explain the protrusion-myosin coupling we observe without invoking more complicated hypotheses requiring RhoA activation or other chemical signaling.

Intracellular myosin distribution depends on phosphorylation of myosin regulatory light chain

Our conceptual model predicts that increasing the effective binding affinity of myosin II to F-actin would increase the rearward localization of myosin II (Figures S2F-S2H). We set out to test this hypothesis experimentally. The interaction of myosin II with F-actin is regulated by the phosphorylation of myosin regulatory light chain (MRLC) at serine 19, a highly conserved residue whose phosphorylation is sufficient to induce a conformational change that favors myosin filament assembly (Craig et al., 1983; Smith et al., 1983). In contrast, myosin II molecules containing non-phosphorylated MRLC exist in a configuration that only binds actin weakly and cannot efficiently form filaments. Increasing the phosphorylation of MRLC should increase the fraction of total myosin that can bind to F-actin and also trigger the assembly of myosin thick filaments (Smith et al., 1983) with tens of actin-binding myosin motor heads (Niederman and Pollard, 1975), which would further increase the effective binding affinity of the myosin for the actin network.

We used several strategies to change S19 phosphorylation. S19 on MRLC is primarily phosphorylated by the myosin light chain kinase (MLCK) (Pearson et al., 1984) and dephosphorylated by phosphatase PP1 with its regulatory myosin-binding subunit MYPT1 (Kimura et al., 1996) (Figure 3A). The small GTPase RhoA activates the kinase ROCK1, which phosphorylates MRLC directly, and also inhibits MYPT1 (Kimura et al., 1996). In HeLa cells, microtubules have been shown to regulate MRLC phosphorylation by

sequestering GEF-H1, a guanine nucleotide exchange factor of RhoA GTPase (Krendel et al., 2002). ROCK1 inhibition by siRNA or Y27632 treatment decreases MRLC phosphorylation and suppresses the binding between actin and myosin (Niggli, 1999). Depolymerization of microtubules in neutrophils results in activation of Rho GTPase and hyperphosphorylation of MRLC (Niggli, 2003). Thus, several components along the MRLC phosphoregulation pathway can be perturbed by small molecule inhibitors or siRNAs to alter the phosphorylation of MRLC. We chose a dosage of Y27632 and the microtubule depolymerizing drug nocodazole that decreased the cell speed by 50% (Figures S3A-S3D). We also used siRNAs to knock down GEF-H1 (Figure 3B), ROCK1 (Figure 3C), or MYPT1 (Figure 3D). To compare the localization patterns of our MRLC-mApple construct with the phosphorylated form of endogenous myosin light chain, we performed immunolocalization with antibody specific for the serine-19 phosphoepitope of MRLC (Figures 3G, S3E-S3G). The overall distribution of pS19-MRLC is similar to that of MRLC-mApple in live imaging under both standard conditions and drug perturbations (Figures 3G, S3E-S3G). Therefore, the myosin localization score calculated by quantifying MRLC-mApple localization can serve as a reasonable proxy for localization of active myosin II filaments.

Consistent with our prediction, ROCK1 knockdown or Y27632 treatment resulted in near-uniform distribution of myosin (Figures 3E-3G). In contrast, increasing MRLC phosphorylation by MYPT1 knockdown or nocodazole treatment resulted in enhanced localization of myosin to the rear (Figures 3E-3G). The myosin localization phenotype resulting from nocodazole (32 μM) could be largely suppressed by GEF-H1 knockdown, suggesting that microtubule depolymerization regulates myosin localization in HL60 cells primarily through GEF-H1 (Figures 3F and 3G). Overall these results are consistent with the predictions of our quantitative model, that enhancing the association of myosin II filaments with the flowing actin network should also enhance rearward localization of myosin II in rapidly migrating cells.

Myosin II motor activity is dispensable for front-rear coupling, but affects leading edge dynamics and migration persistence

In most amoeboid cells, myosin contraction is believed to be a major contributor to the retraction of the cell rear (Lammermann et al., 2008; Uchida et al., 2003). In neutrophils, however, we have observed that enhanced rear retraction occurs in response to acceleration at the leading edge faster than accumulation of myosin can be observed. So far, our observations have focused primarily on myosin localization rather than on motor activity per se. Therefore, we decided to further dissect the role of myosin II motor activity in front-rear coupling. We inhibited myosin II activity by inhibiting ROCK1 activity using siRNA knockdown or Y27632 treatment, or direct inhibition of the myosin II ATPase with blebbistatin, which inhibits the phosphate release of myosin ATPase and reduces the myosin contraction rate without interfering with the weak binding of myosin to F-actin (Kovacs et al., 2004). We analyzed the movement of myosin-inhibited HL60 cells (Figure 3H) as we did for control HL60 cells in Figure 1. In ~50% of ROCK1 knockdown cells and blebbistatin-treated cells, myosin localization at the cell rear was decoupled from the protrusion of the front, with no significant positive cross-correlation at any time lag (Figure 3H). In the blebbistatin-treated cells, the remaining cells that still had some weak coupling between

protrusion and myosin localization exhibited a highly variable temporal response of myosin (Figure 3H). However, under both perturbations, the protrusion speed and the retraction speed were still coupled with no temporal offset (Figure 3H), suggesting that myosin contractility is not required to mediate this instantaneous front-rear coupling. This result further strengthens the plausibility that membrane tension could be the primary mediator of front-rear coupling in migrating HL60 cells.

Although myosin II motor activity was dispensable for the rapid front-rear coupling, inhibition still notably affected other aspects of leading edge dynamics, such as persistence and lamellipodial shape. HL60 cells, similar to primary neutrophils (Hartman et al., 1994), undergo frequent re-orientation and changes of polarity during migration. We observed a significant decrease of lamellipodial persistence in Y27632 or blebbistatin-treated cells or ROCK1 knockdown cells (Figure S3L, M). In addition, myosin-inhibited cells migrated with a narrower leading edge and longer trailing tails (Figure S3J,K,N) (Niggli, 1999). In contrast, nocodazole-treated cells had an equal reduction in cell speed (Figure S3A-S3D), and the cell bodies were rounder with shorter tails, but the width of leading edge did not change (Figure S3J,K,N).

To investigate how myosin II motor activity feeds back to the leading edge dynamics, we photo-inactivated blebbistatin (Sakamoto et al., 2005) to transiently activate myosin contraction at the cell rear. Since blebbistatin does not interfere with the weak binding between myosin and F-actin (Kovacs et al., 2004), myosin II still localizes to the rear of blebbistatin-treated cells. Therefore, we could apply short pulses of blue light to blebbistatin-treated cells to rapidly restore myosin contractility, and observe the interaction between the rear and the front. Immediately after the light pulse, we observed a rapid increase of retraction speed. The protrusion speed also increased and the lamellipodia became progressively wider (Figure 3I-3K, Movie S3). To examine the effect of persistent global myosin II hyperactivation on the dynamics of the leading edge, we used nocodazole, which as described above causes strong myosin localization at the rear (Figures 3F-G). Importantly, the lamellipodia of nocodazole-treated cells became much more persistent under basal condition with uniform fMLP, with each protrusion lasting twice as long as those of untreated control cells (Figure 3L). Furthermore, the cell trajectories were straighter, as quantified by the longer memory of the migration direction (Figure 3M). All of these findings suggest that myosin II contraction does feed back positively to the leading edge dynamics by increasing the persistence and width of the lamellipodia, leading to more persistent cell movement.

Myosin II motor activity mediates rapid flashes at the cell rear

A prominent feature of the myosin II dynamics observed in migrating HL60 cells is the appearance of rapid myosin “flashes” at the cell rear, where myosin accumulation is quickly followed by rapid myosin delocalization (Movie S4). These flashes primarily occurred during changes of cell speed and direction (Figures 4A-4D). Each myosin flash appeared to be a distinct round of accumulation and disassembly that was spatially and temporally discontinuous from the subsequent flashes (Figure 4B), and myosin flashes were most

prominent when cells turned through large angles (Figure 4D). We therefore examined how myosin accumulation might be associated with these features of cell migration.

We asked how the accumulation and disassembly of myosin is related to its underlying F-actin substrate. To image local myosin and F-actin dynamics simultaneously, we generated an HL60 cell line stably expressing MRLC-mApple and Lifeact-mEmerald, a marker for F-actin (Riedl et al., 2008). Within each flash, the F-actin and myosin II dynamics closely mirrored each other, as shown by the local fluorescence intensity maps (Figure 4E) as well as individual fluorescent images (Figure 4F), suggesting simultaneous accumulation and disassembly of the actin-myosin complex. We quantified multiple flashes and obtained average dynamical patterns. During each retraction, membrane retraction started before visible accumulation of F-actin and myosin II. Within 10 sec, local F-actin and myosin concentrations started rising simultaneously. Both F-actin and myosin II local intensity reached a peak level of about 3-fold higher than the basal level. After that, both F-actin and myosin were disassembled simultaneously, and returned to basal level within 1 min after the onset of membrane retraction (Figure 4G).

To examine how myosin contraction affects the actin-myosin flashes, we chose a dosage of blebbistatin (10 μM) that has a modest, sub-maximal effect on myosin contractility. We observed a longer time lag for the increase of myosin concentration following the initial membrane retraction, and a two-fold increase of the duration and amplitude of the myosin flashes, as compared to untreated control cells (Figures 4G-4I). While the disassembly process typically started when myosin reached 3-fold above basal level in untreated cells, the threshold rose to 5-fold above basal level under blebbistatin treatment. These results indicate that myosin II motor activity is important both in mediating the rapid accumulation of the actin-myosin complex and in driving the subsequent transition into the disassembly phase. Consistent with our model, stabilizing actin filament with jasplakinolide also increases the duration of myosin flashes but the effect is milder than inhibition of myosin contraction with blebbistatin (Figure 4J).

We next examined RhoA activity locally at the sites of membrane retraction, using the FRET sensor described above, and observed large fluctuations near the retracting edge of the cell. We analyzed the temporal coupling between rapid local variations in RhoA activity and the local edge retraction velocity, just before the time we see the myosin II flashes. The temporal offset between local RhoA activity and local edge retraction velocity was not reproducible from one cell to another (Figure S4). This is in sharp contrast to the highly reproducible time lag of 5-10 sec between local retraction velocity and local myosin concentration (Figures 4G and 4I). This data suggested that variations in RhoA activity are unlikely to trigger the myosin flashes directly.

Finally, we observed a positive correlation between MRLC phosphorylation and the duration of the flashes. Perturbations that increased MRLC phosphorylation, such as MYPT1 knockdown and nocodazole treatment, increased the duration of myosin flashes, while decreasing MRLC phosphorylation by ROCK1 knockdown shortened the duration (Figures 4K and 4L). Note that the phenotype of prolonged myosin flashes was more extreme under nocodazole treatment than MYPT1 knockdown.

Asymmetric myosin II localization follows the directional change of protrusion to facilitate efficient turning

Having established this basic framework to understand the interactions among protrusion, retraction, and myosin localization along the front-rear axis, we next asked whether we can extend our quantitative analysis to a turning cell, when the front-rear axis rotates in 2D. Based on our model (Figures 2H-2K and S2), we expect that a cell undergoing a change in direction at the leading edge should accumulate myosin II at the new presumptive trailing edge (formerly one side of the cell) about 9-15 seconds later, and that left-right asymmetry of myosin II localization should be correlated with the angular speed of the cell, again with a similar temporal offset. We developed a metric to quantify the turning angle of the cell, emphasizing the difference between the direction of the front and the rear of the cell, and compared it to a metric for left-right asymmetry of myosin distribution (Figures 5A-5C, S5, Movie S5, and Methods). Under standard migration conditions, we noticed that the leading edge was highly dynamic and exhibited frequent change of directions, while the uropod changed direction less dramatically and over a longer characteristic time scale (Figure 5D).

We compared the turning angle of the cell versus myosin asymmetry in single cell trajectories (Figure 5E) and over population averages (Figure 5F). Consistent with our earlier observation of the temporal offset between cell acceleration at the front and the rearward accumulation of myosin, the left-right asymmetry of myosin lagged behind the directional change of the protrusion by ~ 15 sec.

This temporal analysis of various parameters during cell turning (Figures 5E and 5F), supports a simple mechanical model, drawn to summarize a single turning event in Figure 5G. At the beginning of a turning event, the protrusion initiates the directional change. The turning angle increases when myosin is still symmetric (Figure 5F and 5G step 1). As the turning angle increases, the retrograde flow of actin, and therefore also of the myosin, effectively rotates towards the outside of the turning cell in the cell frame of reference (the right side in the diagram), and results in the increase of myosin left-right asymmetry about 15 sec after the initiation of the turn (Figures 5F and 5G step 2). The asymmetric distribution of myosin leads to a faster retraction at the right side of the cell, causing the uropod to rotate towards the right, and into better alignment with the front. The rotation of the uropod decreases the turning angle (Figures 5F and 5G step 3). As the front and back are aligned, the myosin retrograde flow becomes symmetric and the asymmetric accumulation of myosin stops, leading to a reduction of myosin left-right asymmetry (Figures 5F and 5G step 4). Finally, the intrinsic disassembly mechanism of a myosin flash further removes the residual myosin asymmetry and allows the cell to migrate towards the new direction set by the front of the cell (Figures 5F and 5G step 5). Thus, we propose that the asymmetric accumulation of myosin driven by the actin-dependent rearward transport forms a negative feedback to correct for the mismatch between front and back directions and promote efficient turning and directional change. In this way, a chemotactic HL60 cell can re-orient itself efficiently following the directional decision made by the leading edge.

Using TIRF measurements of myosin retrograde flow in turning cells, we directly observed these processes in a single cell (Figures 5H-5J and Movie S6). In the example shown, the overall cell directional reorientation takes about 3 min. The turning event is initiated by a

change in the angle of cell protrusion, which is immediately reflected in a change in the direction of the retrograde flow of myosin II puncta, with reorientation of the uropod lagging behind. This sequence of events suggests that the direction of actin flow, as determined by the geometry of cell protrusion, can be efficiently communicated to the rear of the cell by this myosin II transport mechanism. Once there, the accumulated myosin II at the new presumptive rear can contribute to reorientation of the uropod via contraction and depolymerization of the local actin network on the outside rear edge of the turning cell.

Rapid myosin dynamics is preserved in HL60 cells forced to turn mechanically, and facilitates quick re-orientation of the rear during chemotaxis

Our analysis suggests that a simple mechanical model is sufficient to describe the observed myosin dynamics for cells changing directions spontaneously (Figure 5G). Next we wished to test whether myosin would behave similarly for cells that are forced to turn in a particular direction. We designed a microfluidic channel (Boneschansker et al., 2014; Irimia, 2014) that forces migrating HL60 cells to turn with a predefined 90 degree angle, and observed the corresponding myosin dynamics (Figures 6A, B and Movie S7). Similar to HL60 cells migrating freely under agarose (Figure 5E), cells migrating in the channel exhibit a comparable lag of ~15 sec between the change of protrusion direction and the left-right asymmetry of myosin (Figure 5C-5E). The similarity of myosin dynamics during cell turning between freely migrating HL60 cells and HL60 cells mechanically forced to turn further support the sufficiency of our model.

To further investigate the significance of rapid myosin dynamics in cell turning, we asked how changes in myosin dynamics could affect the turning dynamics of neutrophils migrating towards a physiologically relevant point source, *Candida albicans*. *C. albicans* is among the most common species of fungal infection in neutropenic patients (Safdar et al., 2001). Neutrophils are the primary immune cells to target *C. albicans* infection and clear these pathogens by phagocytosis (Mansour and Levitz, 2002). HL60 cells differentiated by DMSO have been shown to reverse candidiasis in neutropenic mice (Spellberg et al., 2005), suggesting that the DMSO-differentiated HL60 cells are reasonable model system to study the clearing of *C. albicans* by primary neutrophils. When we mixed the HL60 cells with *C. albicans* in an under-agarose assay, we observed that HL60 cells migrated towards the fungal cells and then phagocytosed them (Figure 6F, 6G and Movie S8). We observed flashes of myosin in the re-orienting HL60 cell rear as the cell approached the fungal cell, similar to those observed in the absence of *C. albicans* and the presence of uniform fMLP (Figures 4A-4D and Movie S4). Importantly, we frequently noticed that some HL60 cells needed to turn sharply to correct their trajectories as they closely approached the fungal cell (Movie S8). This sharp turning allowed us to analyze how the directions of protrusion, retraction, and myosin were aligned during neutrophil chemotaxis in the final stages of attack on this pathogenic fungus (see Methods) (Figures 6F-6K). We found that the protrusion always led the turn and aligned with the *C. albicans* before the rear of the cell did. In the control HL60 cells, the response time of myosin contraction and membrane retraction to the final protrusion towards the *C. albicans* were both less than 20 sec (Figure 6L and 6M, and Methods). Among all the perturbations we tested (Figure 3A), nocodazole treatment generated the most extreme phenotype on myosin dynamics and localization. Therefore, we

focused on characterizing the turning dynamics towards *C. albicans* cells under nocodazole treatment. When nocodazole-treated HL60 cells approached the fungal cell, the myosin cluster remained stable and did not exhibit dynamic re-localization. Instead, it appeared to be passively dragged by the protrusion and only gradually turned towards the fungal cell (Figure 6G and Movie S8). Consequently, it took three times longer for the contracting myosin to align with the front in nocodazole-treated cells as it did in untreated control cells (Figure 6L and 6M). This lag of myosin response seen in nocodazole treatment could be rescued by GEF-H1 knockdown (Figure 6L), suggesting that the slow myosin response can be attributed to the hyperphosphorylation of MRLC. Importantly, the response time of membrane retraction was not perturbed significantly, even under nocodazole treatment, consistent with myosin not being the sole contributor to the retraction of the cell rear. Once again, our results showed that the rapid myosin dynamics facilitates the quick response of myosin to the directional change at the front and allow the whole cell to re-orient efficiently, even under a chemotactic process towards a physiologically relevant point source.

Efficient front-rear coupling and dynamic myosin II localization can be observed for migrating neutrophils *in vivo*

Finally, we compared our observations on HL60 cells to primary neutrophils migrating in 3-day-old zebrafish larvae *in vivo*. We used transgenic zebrafish co-expressing myosin light chain-EGFP with mCherry or Lifeact-Ruby under a neutrophil-specific promoter lysozyme C (*lyz*) (Kitaguchi et al., 2009; Lam et al., 2012), and acquired time-lapse confocal images of migrating neutrophils *in situ* (Lam et al., 2014). The overall shape of primary neutrophils *in vivo* was substantially more complex than HL60 cells in culture, however most cells moved fairly persistently (Movie S9). We analyzed the protrusion and retraction dynamics similar to our analysis in HL60 cells (Figures 7A-7C). As in the HL60 cells, the protrusion and retraction speed of neutrophils in zebrafish larvae fluctuated dramatically over time (Figures 7A and 7B). Importantly, despite the large-amplitude fluctuations, the protrusion and retraction speed of zebrafish neutrophils were still instantaneously coupled without any time lag (Figures 7B and 7C). In addition, myosin flashes at the retracting rear of zebrafish neutrophils were readily observable (Figures 7D-7F and Movie S9). We quantified 11 retraction events in 4 neutrophils from 3 zebrafish larvae. On average, the myosin flashes in zebrafish neutrophil last about 30 seconds, and reach a peak intensity at about 3 fold of the basal concentration (Figure 7G), very comparable to what we observed in HL60 cells (Figure 4G). When compared with local edge retraction velocity, local myosin dynamics lag behind the retraction velocity by 5-10 sec (Figure 7H). These features of the myosin flashes in zebrafish neutrophil agree not only qualitatively, but also quantitatively with our measurements in HL60 cells. The conservation of the rapid response of myosin to membrane retraction and the short-lived myosin pulses could reflect a universal timescale determined by the interaction between actin and contractile myosin filaments for rapidly moving neutrophil-like cells, regardless of their physical environment.

DISCUSSION

In this study, we have shown that membrane protrusion at the front and retraction at the rear of a migrating neutrophil are instantaneously coupled to achieve efficient chemotaxis. The

initial instantaneous response is mediated by a myosin and RhoA signaling-independent mechanism, such as membrane tension. Membrane retraction induces a rapid cycle of myosin assembly and disassembly to facilitate further contraction and re-orientation of the rear, and enable persistent front protrusion and efficient turning. This mechanism appears to operate in neutrophil migration in the presence or absence of chemoattractant gradient in a 2D tissue culture model under confinement, as well as migration of primary cells in 3D *in vivo*.

Several layers of biochemical and mechanical feedback have been shown to enable a neutrophil to perform chemotaxis efficiently (Houk et al., 2012; Wang et al., 2002; Weiner et al., 2002; Wong et al., 2007; Xu et al., 2003). Our work has identified an additional layer of mechanical coupling, mediated by myosin II accumulation and contraction, through which the front and back are positively mutually reinforcing. As the actin polymerization rate at the front of the cell increases in the context of an overall acceleration or reorientation during a turn, the combination of accelerated retrograde flow and rear myosin II-driven contraction leads to a rapid increase of myosin II accumulation at the rear. Therefore, the front module reinforces the back module mechanically. The increase of myosin contraction at the rear increases the persistence and width of lamellipodia at the front. Therefore, the back module also reinforces the front module. The mechanical reinforcement could serve as a coupling mechanism that operates faster than biochemical signaling to allow efficient movement of the whole cell and maintain appropriate alignment between the lamellipodium and the uropod.

The geometry of cell migration assays could affect the observed phenotypes. However, the mechanism of front-rear coupling shown in this work should be generally applicable to other confined environments. Our basic observations that protrusion and retraction are instantaneously coupled, that myosin II puncta are transported in the cell frame of reference by actin retrograde flow, and that membrane retraction induces transient myosin flashes, should hold true in a wide variety of different external geometries. In this work, we provided examples of HL60 cells migrating under agarose and in microfluidic channels, and also primary neutrophils migrating in zebrafish larvae. Recent evidence has shown that neutrophil-like amoeboid movement could be the predominant migration mode for a wide range of cell types when they are under confinement and low adhesion conditions (Liu et al., 2015). In this mode of migration, even mesenchymal cells or cancer cells could exhibit strong actin flow with retrograde transport of myosin II. Therefore, the mechanisms described in our work could be a universal feature for efficient front-rear coupling in cells migrating in confined and low-adhesion environments.

STAR METHODS

CONTACT FOR REAGENT AND RESOURCE SHARING

For all requests for reagents and resources used in this paper, please contact Julie Theriot (jtheriot@uw.edu) at the University of Washington.

EXPERIMENTAL MODEL AND SUBJECT DETAILS

Culture of HL60 cells—The HL60 cell line (derived from a 36 year-old female) was a generous gift from Orion Weiner's lab (Weiner et al., 2007). HL60 cells were maintained in RPMI media (Invitrogen 22400), supplemented with 10% fetal bovine serum (FBS) (Gemini), antibiotic and antimycotic drugs (GIBCO 15240). The cultured cells were diluted once every 3-4 days into a density of 10^5 cells/ml. To differentiate the HL60 cells, cells were diluted to RPMI full media containing 1.3% DMSO (Acros 61097) with an initial density of 2×10^5 cells/ml. For all the experiments, only cells differentiated for 5-6 days were used.

Generation of HL60 cell lines stably expressing Actin-YFP and MRLC-mApple —HL60 cells expressing actin-YFP were obtained from OrionWeiner's lab (Weiner et al., 2007). To construct MRLC-mApple, we started from a template with mApple (Genbank DQ336160.2) fused to the N-terminus of myosin regulatory light chain (Genbank BC055439.1), and cloned the myosin regulatory light chain –mApple in a lentiviral packaging plasmid FG46013. The lentiviral vector FG46013, derived by combining pTRIPZ and FG12 at *Sap*I sites, was a generous gift from Dr. Xuedong Liu from University of Colorado - Boulder. The plasmid, together with three other helper plasmids containing gag, pol, and rev genes were transfected to HEK293 cells at 25% confluence. The virus-containing supernatant was harvested 48 hours later, and concentrated 100 fold with Amicon Ultrafuge Filter. 10^6 HL60 cells were infected with 300 μl of concentrated virus supernatant by centrifuging under 1000xg for 2 hours. Polybrene (hexadimethrine bromide) was added at a final concentration of 10 μg/ml to increase infection efficiency. The infected cells were sorted by FACS at least three days after infection.

Generation of transgenic zebrafish—Zebrafish (*Danio rerio*) AB strain was used throughout. Adult zebrafish were maintained on a 14 h light / 10 h dark cycle at ~28°C. Zebrafish embryos were obtained by crossing male and female adults aged 3-18 months. Embryos were maintained in E3 medium with 1% Methylene Blue (Sigma-Aldrich) at 28.5°C. 0.003% 1-phenyl-2-thiourea (PTU; Sigma-Aldrich) was added to E3 started at 24 hours post fertilization to reduce pigmentation of embryos. A detailed description of zebrafish embryo injections has previously been described(Lam et al., 2014). In short, DNA expression vectors contained the zebrafish lysozyme C (*lyz*) promoter for neutrophil-specific expression (Kitaguchi et al., 2009; Lam et al., 2012). All expression vectors contain minimal Tol2 elements for efficient integration (Urasaki et al., 2006) and an SV40 polyadenylation sequence (Clonetech Laboratories, Inc.) for mRNA stabilization. *lyz-MRLC2-EGFP* (*Homo sapiens* myosin light chain 12B, accession NM_001144944) was generated for visualizing myosin light chain subcellular localization. Transient mosaic expression of the construct was obtained by injecting 3 nL of solution containing 12.5 ng/μL of DNA plasmid and 17.4 ng/μL *in vitro* transcribed (Ambion) Tol2 transposase mRNA. Injections were made into the cytoplasm of one-cell stage embryos of either *Tg(lyz-mCherry)* or *Tg(mpx:Lifeact-Ruby)* (Yoo et al., 2010) transgenic line. All animal studies were approved by the University of Wisconsin-Madison Animal Care and Use Committee (Protocol number: M01570-0-02-13) and performed in accordance with the guidelines.

METHOD DETAILS

Microscopy—To image single cell actin-myosin dynamics with high spatiotemporal resolution, we used a Nikon Diaphot 300 epifluorescent microscope with a 1k back-thinned EM-CCD camera, Andor iXon3 (Andor). A temperature and humidity control unit (Haisen Tech) was installed with the microscope to maintain constant temperature at 34°C. The TIRF microcopy was performed on a Zeiss TIRF Axiovert microscope with Hamamatsu Image EM EM-CCD camera (Hamamatsu). To image cell migration trajectories under various concentrations of chemical inhibitors in a 96 well high-throughput format, we used the ImageXpress Micro (Molecular Devices). The microscopy setup and the image analysis method for the RhoA FRET sensor were previously described (Yang et al., 2015). In short, cells were imaged using a custom-assembled spinning disc confocal/epifluorescence microscope system built on a Zeiss Axiovert 200M microscope with a 40x (1.3 numerical aperture) objective at 37°C. To avoid artifacts from sequential acquisition of two image channels in fast moving cells, an Optical Insights Dual-View beam splitter (Photometrics) were used for simultaneous acquisition of CFP and FRET channels.

Zebrafish *in vivo* neutrophil imaging was previously described (Lam et al., 2014). In short, larvae at 3 dpf were anesthetized using 0.2 mg/mL tricaine and mounted on a glass-bottom dish with 1% low melt agarose for live imaging. All images were acquired using a spinning disk confocal microscope (Yokogawa CSU-X) with a confocal scanhead on a Zeiss Observer Z.1 inverted microscope (NA1.3/60X water immersion objective) at 28.5°C. A Photometrics Evolve EMCCD camera was used to acquire the images. Z-series images were acquired using a 0.4 μM step size and 300 EM gain. Time intervals between each Z-stack images range from 6.17 s to 22 s. We selected neutrophils that were predominantly migrating within the *x-y* imaging plane with minimal *z* displacement.

Under-agarose cell migration assay—To make the agarose pad, we first prepared a 2x stock solution of L-15 media (Gibco) with 20% fetal bovine serum (Solution A). For the chemokinesis assay, fMLP (Sigma F3506) was added to Solution A at a final concentration of 2 nM. For the *Candida* assay, no fMLP was added. The chemical inhibitors, when used, were added to 2x final concentration. Secondly, we made Solution B by dissolving 2% low melting point agarose (Invitrogen 16520) in heated L-15 media, and kept in a 37°C water bath until use. Solutions A and B were mixed at a 1:1 ratio and added to a mold to generate agarose pads. For regular time-lapse imaging, we used agarose pads with a thickness of ~2 mm. The agarose was kept at room temperature for at least 20 min to solidify. 10^5 cells were spun down with 500xg for 5-10 min, and then concentrated to a final concentration of 10^4 cells/μl. 10 μl of the concentrated cell solution was added to the center of a coverslip, coated with 10 μg/ml fibronectin (Sigma F2006). The solidified agarose pad was overlaid above the 10 μl cell solution. The coverslip was placed in a microscope adapter and then used for time-lapse imaging. Typically, the agarose pad would start compressing the cells within 20 min. When the cells were fully confined under the pad (Figure S1A and S1B), the cell area increased, and the brightness of the halo around the cell decreased in phase contrast images. We only started imaging after the cells were confined. At this level of confinement, the cell would stay in the imaging plane throughout the time-lapsed movies and the subsequent

shape analysis is very simple and reliable. The temperature was maintained at 34°C with a temperature control chamber (Haisen Tech).

Microfluidic Assay—At the beginning of each experiment the microfluidic device was primed with 100 nM f-MLP diluted in Solution A (as previously described). The device was placed in a desiccator connected to house vacuum for 10 minutes to ensure the full removal of air pockets from the migration channels. As the air was displaced the chemoattractant filled the array of migration channels connected orthogonally to the central loading channel. The device was washed twice with 10 μg/ml fibronectin diluted in Solution A. The washing steps created a chemokine-free environment at the central loading channel, which served as a sink. The passive diffusion of chemoattractant from the migration channels into the central loading channel established a chemoattractant gradient. 10 μl of cells concentrated down to 10^4 cells/μl were loaded into the device. Cell migration in the direction of the chemoattractant gradient commenced immediately. Images were captured every 2.5 seconds using a 100x oil immersion objective. The temperature was maintained at 37 °C.

Chemical inhibitors, siRNAs, and antibodies—For each chemical inhibitor we used, we first obtained a dose-response curve on cell speed by microscopy using an ImageXpress Micro (Molecular Devices). For the purpose of cell tracking, the cells either were stained with DRAQ5 (Cell Signaling) or were expressing cytoplasmic GFP. Images were taken at 20x magnification with 1 min intervals. For each concentration of drug, we obtained more than 100 single cell trajectories over 30-60 min. The average speed was determined by dividing the total path length by the duration of migration. For the experiments performed with chemical inhibitors, we chose a dosage corresponding to 50% reduction of cell speed. Specifically, we used 32 μM nocodazole (Sigma M1404), 5 μM Y27632 (Calbiochem 688000), and 10 μM (−)-blebbistatin (Fisher scientific). siRNAs were ordered from Dharmacon (siGENOME set of 4), targeting GEF-H1(MQ 009883-01-0002), ROCK1 (MQ 003536-02-0002), and MYPT1(MQ 011340-01-0002). As a control siRNA, we used the siGENOME non-targeting siRNA pool #2 (D-001206-14-05). HL60 cells differentiated by DMSO for 3 days were electroporated with the siRNA using a 96 well plate format electroporator(Guignet and Meyer, 2008). The migration experiments and Western blotting, to evaluate the knockdown efficiency, were done 3 days after siRNA electroporation. ROCK1 (sc-6056) and MYPT1 (sc-17434) antibodies were obtained from Santa Cruz Biotechnology. The GEF-H1 antibody was obtained from Cell Signaling (4145). MAPK was detected with a polyclonal antiserum (X15) raised against a 12-amino acid peptide from the *Xenopus* p42 MAP kinase sequence (IFEETAEFQPGY) conjugated through an amino-terminal cysteine residue to bovine serum albumin (Hsiao et al., 1994).

Immunofluorescence of phosphorylated myosin light chain in HL60 cells—Differentiated HL60 cells were first prepared for the under-agarose 2D migration assay, with specific chemical inhibitors (using DMSO as control) being applied to the cells via a thin agarose pad (see section on “Under-agarose cell migration assay”). After the cells were fully confined, cell migration was allowed to continue under agarose for 15 min before 1 mL of cytoskeleton buffer (CSK: 100 mM HEPES, pH 7.0, 138 mM KCl, 3 mM $MgCl_2$, 2 mM EGTA, and 320 mM sucrose), containing 3.7% formaldehyde and 0.05% glutaraldehyde,

was added directly on top of the agarose pad, followed by a fixation period of 20 min. The CSK buffer was then aspirated and replaced with 1x phosphate-buffered saline (PBS), and the agarose pad was allowed to self-detach from the coverslip with minimal mechanical disturbance.

The fixed cells were then immunostained by first being washed twice with 1x PBS, followed by membrane permeabilization using 0.5% Triton X-100 in 1x PBS for 10 min. A second wash was then performed using 0.1% Triton X-100 in 1x PBS before the cells were incubated with a blocking solution (PBS-BT: 3% BSA, 0.1% Triton X-100, and 0.02% sodium azide in 1x PBS) for 30 min. We used a primary antibody targeting the phosphorylated serine-19 (pS19) epitope of the myosin regulatory light chain (MRLC) (ab2480, Abcam). Note that this antibody will recognize the phosphorylated serine-19 of MRLC3 and phosphorylated serine-20 of MRLC2. Both forms of MRLC are highly expressed in the HL60 cells. A 90-min incubation with the primary antibody was performed at 10ug/ml in 1x PBS-BT, followed by three 7-min washes using 1x PBS-BT. Secondary antibody incubation of 60 min was then performed using a goat anti-rabbit Alexa Fluor 488 fluorochrome-conjugaed antibody at 2ug/ml in 1x PBS-BT (A11008, Life Technologies). The cells were then washed with 1x PBS three times before being imaged under the same settings as the under-agarose 2D cell migration assay.

Candida albicans* assay—Candida albicans* (strain SC5314) was obtained from the American Type Culture Collection (ATCC). The *C. albicans* was grown from frozen stock in an overnight culture of YPD media for > 12 h in dark at 30°C. The density of HL60 cells and *C. albicans* were determined right before the experiment. The *C. albicans* were harvested and washed twice, first with PBS and then with RPMI media, by centrifugation and resuspension. 10^5 HL60 cells and 5×10^4 *C. albicans* cells were each concentrated in 10 μl of RPMI media. The two cell solutions were then mixed, immediately added to the center of a fibronectin-coated coverslip, and overlaid by the agarose pad. Since we were interested in the turning phenotypes, we only included cells that undergo an obvious turn to approach the *C. albicans* in our analysis. For each frame of a movie, we calculated the points along cell boundary with the maximal protrusion speed, the maximal retraction speed, and the maximal myosin intensity. We then connected these three points with the cell centroid, and defined these three vectors as the directions of membrane protrusion, membrane retraction, and myosin contraction (Figures 6F and 6G). We compared how these three directions change relative to each other (Figures 6H and 6J), and calculated the differences between the protrusion and the retraction, and between the protrusion and the myosin contraction (Figures 6I, 6K-M). We defined the response time of myosin as the first time that the myosin aligned with the protrusion during the last turn towards the *C. albicans* cell (Figures 6I and 6K magenta arrow and Figure 6L). A similar analysis was performed between the protrusion and the membrane retraction direction to obtain the response time of membrane retraction (Figure 6M).

QUANTIFICATION AND STATISTICAL ANALYSIS

Image analysis and calculation of migration parameters—Precise segmentation of cellular boundaries is critical in our work. Empirically, we found that manual user correction

was necessary to ensure the quality of segmentation. We developed a semi-automatic workflow using the magnetic lasso and quick selection tool in Adobe Photoshop CS6 (Adobe Systems Inc.) to enable fast manual segmentation. Segmented cell masks were processed using Celltool, developed by Zachary Pincus (Keren et al., 2008; Pincus and Theriot, 2007), to convert each mask into 300 equally spaced grid points along the circumference. Comparison of cell shapes was performed using principal components analysis as previously described (Keren et al., 2008).

For every frame, we calculated the centroid of the whole cell, and obtained the velocity of the cell centroid. To calculate the protrusion and retraction speed, we compared the cell contours in consecutive frames, and marked the newly-protruded regions and the newly-retracted regions. To avoid segmentation error and only include true protrusions and retractions, we set an empirical cut-off threshold of 100 pixels (1.2 μm^2) and discarded regions that were smaller than this threshold. The area of the remaining regions was summed up to obtain the instantaneous protrusion speed and retraction speed. An illustration of the analysis is shown in Movie S1.

To calculate the myosin rearward localization score, we first defined a front-to-rear axis at each frame. We started at the cell centroid, and extended a vector along the direction of the centroid movement (Figure S1C). We then found the intersection of this extended vector with the cell contour, and identified a point from the 300 grid points closest to this intersection. We numbered this point −75, and sequentially increased the index from −74 to 75 on both sides (Figure S1C). At each grid point with index i, we defined a box with a width of 6 grid points (~0.9 μm), and a depth of 1μm, and calculated the average fluorescent intensity within this box, and defined it as M_i. The myosin rearward localization score is defined by $(\sum i^* M_i)/\sum M_i$, where i starts from −75 in the front of the cell, goes up to 75 along the left boundary of the cell, and goes back down to −74 along the right boundary of the cell (Figure S1D).

To calculate the myosin left-right asymmetry score, we need to take into account that the left and the right boundaries of the cell are often not equal in length, especially when the cell is turning. Therefore, we developed an adapted indexing system. We defined the front of the cell as the point along the cell boundary with the maximal protrusion speed, and defined the back of the cell as the tip of the uropod (Figure S5A). We then calculated the number of evenly-spaced grid points on both sides of the cell, to assign the left of the cell L points and the right of the cell R points. We defined the new indices as follows (assuming for example that L and R are odd numbers): At the left of the cell, the index l starts from −1 to $-(L+1)/2$ and back to −1 (Figure S5). At the right of the cell, the index r starts from 1 to $(R+1)/2$ and back to 1(Figure S5). To account for unequal numbers of grid points on both sides, the indices on the left and right sides were multiplied by scalars α and β, respectively, so the sum of the left indices became −1000 and the sum of the right indices became 1000 (Figure S5B). Finally, the myosin left-right asymmetry score was calculated by the following formula: $(\alpha\sum l^* M_l + \beta\sum r^* M_r)/(\sum M_l + \sum M_r)$. The numerator is the sum of the product of each index with its corresponding myosin intensity. The denominator is the sum of all the myosin intensity in every grid point (Figure S5B). Examples of the myosin left-right asymmetry score are given at Figures 5B and 5C.

Constructing an experimentally-parameterized mathematical model for myosin dynamics—We developed a mathematical framework incorporating our quantitative measurements, with the goal to test whether simple interactions between actin and myosin could account for the myosin dynamics we observed experimentally. We first assumed that the actin filaments were abundant and never became rate-limiting for the myosin-actin interaction. Therefore, we could focus on the spatial distribution of myosin alone. We separated the myosin into a cytoplasmic pool (named free myosin hereafter) and a F-actin bound pool (named bound myosin hereafter) (Figure 2H). Based on our observation in TIRF microscopy, we assumed that the bound myosin is not diffusible, and drifts towards the rear with the retrograde flow, in the cell frame of reference. The velocity of the retrograde flow, $V(t)$, is equal to the cell speed, which typically fluctuates from 5 to 10 μm/min. The cytoplasmic myosin could diffuse freely, with a diffusion coefficient D. We measured the diffusion coefficient of cytoplasmic myosin by fluorescence recovery after photobleaching (FRAP) (Figure S2A-S2C). To ensure the majority of the myosin molecules measured by this technique were cytoplasmic, we treated the cells with Y27632 (5 μM) to inhibit the binding of myosin to F-actin. We obtained a diffusion coefficient of 0.13 ±0.07 μm^2/sec (N=5). Note that we were still underestimating the diffusion coefficient because we did not consider the lack of fluorescent myosin molecules on one side of the photobleached region due to the presence of the cell membrane.

We took a data fitting approach to estimate the binding kinetics between myosin and F-actin. We started by using the experimentally measured value for the velocity of the retrograde flow (V=7 μm/min) and the diffusion coefficient (D=0.13 μm^2/sec), and ran the simulation with different combinations of k_{on} and k_{off} (Figure S2D). For each set of parameters, we tracked the myosin intensity of a point as it moved towards the rear of the cell, and fit the simulated data with an exponential curve to obtain the doubling time (Figure S2E). Note that the increase of myosin intensity can be well-fit with an exponential curve, further confirming the consistency of the model with our experimental observation (Figure 2G and Figure S2E). Based on the results of our simulation, there is a curve in the 2D k_{on} - k_{off} map that fits the 40 sec doubling time of myosin intensity (Figure S2D). We first selected k_{on}=0.3 min^{-1} and k_{off}=0.7 min^{-1} (magenta circle in Figure S2D). After determining the values of all four parameters, we next calculated the response of myosin localization to an imposed oscillatory variation in cell speed. We assumed the cell speed changed from 3.5 μm/min to 10.5 μm/min, with a period of 1.25 min. The period and amplitude of the speed change were estimated from experimental observations (Figure 1B). When comparing the speed change with the myosin localization score, our model generated a response time of 15 sec, as quantified by the cross-correlation analysis (Figure 2I and 2J). Note that we have also carried out the simulation using another parameter set (k_{on}=0.2 min^{-1} and k_{off}=0.2 min^{-1}) that fit the doubling time of myosin equally well (yellow circle in Figure S2D), and also obtained a response time of 15 sec. The model also allowed us to investigate the stability of our simulation results. We varied each of the 4 parameters up and down by 8 fold. The response time of myosin was very stable when each parameter was changed within one order of magnitude, and stayed within 10-20 sec (Figure 2K).

The model also predicted that increasing the binding affinity of myosin to F-actin would increase the rearward localization of myosin (Figure S2F). We extended our model to simulate the effect of myosin localization when phosphorylation of MRLC was perturbed. Perturbing the phosphorylation of MRLC would change the effective k_{on} and k_{off} values in two additive ways. First, it would change the fraction of MRLC molecules that could bind F-actin, and therefore alter the apparent binding affinity at a population level (Figure S2G). Second, phosphorylation of MRLC would trigger assembly of myosin thick filaments (Smith et al., 1983), consisting of tens of motor domains in non-muscle myosin (Niederman and Pollard, 1975). When multiple motor domains exist in the same filament, the filament could bind to F-actin as long as one motor head is bound, resulting in an increase of the effective k_{on} and a decrease of the effective k_{off}. Therefore, the myosin localization score would be expected to increase monotonically as the size of the myosin filament increases (Figure S2H).

Analysis of persistence run duration—We determined the persistence of the cell using two different methods. The lamellipodia can be seen in phase contrast images with a smooth and relatively uniform texture. Therefore, we could determine when a lamellipodium was formed and retracted simply by inspecting the phase contrast images. Within a typical time-lapse movie that lasted 30-60 min, we could observe multiple cycles of lamellipodia initiation and retraction, and record the average protrusion lifetime for each cell. We took into account the lifetime of existing protrusions that were present in the beginning of the movie and at the end of the movie, so that we would not discard the most persistent cells that has one single protrusion throughout the movie. Therefore, there is a systematic under-estimation of the lamellipodia lifetime. To complement our analysis with an automatic algorithm, we determined an empirical speed threshold of 2.1 μm/min that separated a trajectory at the moving phase from a pausing and re-orienting phase (Figure S3L). For each trajectory, we first used a spline-fit tool in MATLAB (Mathworks) to remove noisy speed fluctuations due to image processing error, and only captured the longer timescale fluctuations of cell speed. We then calculated the average duration that each cell stayed in the moving phase, and defined this number as the persistence run time.

Calculation of directional auto-correlation—The directional auto-correlation value is the average $\cos\theta$ value of the angle θ between each velocity vector at time t, v(t), and the velocity vector at time $t+\Delta t$, $v(t+\Delta t)$, with the following formula:

$$\rho(\Delta t) = \frac{\sum_1^{T-\Delta t} cos\theta(t, t+\Delta t)}{T-\Delta t} = \frac{\sum_1^{T-\Delta t} \frac{v(t)\cdot v(t+\Delta t)}{|v(t)|\ |v(t+\Delta t)|}}{T-\Delta t}$$

The longer the cell maintains its migration direction, the higher the directional auto-correlation. A trajectory of a straight line will have a directional auto-correlation value of 1.

Cross-correlation analysis and bootstrapping statistics—We have used cross-correlation analysis throughout the paper to compare temporal dynamics of two parameters and test for statistical significance of the temporal offset. For two time series data

$X(t)=[x_1,x_2,\ldots,x_n]$ and $Y(t)=[y_1,y_2,\ldots,y_n]$. The Pearson correlation of the two time series with offset (Δt) is calculated as follow:

$$\rho(\Delta t) = \frac{\mathrm{Cov}(x(t), y(t+\Delta t))}{\sqrt{Cov(x(t), x(t))Cov(y(t), y(t))}}$$
$$\text{where } \mathrm{Cov}(x, y) = \Sigma_{i=1}^{n}(x_i - \bar{x})(y_i - \bar{y})$$

We used bootstrapping to obtain the 95% confidence interval of each cross-correlation value. We randomly permuted the time traces of x and y, and perform the same cross-correlation analysis to obtain the maximal correlation with all possible temporal offsets. We then repeat this process 2000 times to obtain a distribution of maximal correlation value. The 95% confidence interval indicated a correlation value better than 95% of the maximal correlation values one can obtain with a pair of randomly permuted x and y.

Principal component analysis to obtain principal shape modes—The principal component analysis of cell shape (Figure S3H and S3I) is carried out in the software environment of Celltool. Cells are segmented frame-by-frame to obtain precise cell contours. All the contours are aligned to minimize the total deviations. Cell contours are re-sampled into 300 equidistant points. The shape modes are obtained by principal component analysis from the 600 (300 points with x and y coordinates) dimension data. For visualization purposes, the mean and the mean ± 1 or 2 standard deviations along each principal axes were shown. Shape distribution along the first principal mode was visualized by plotting the mean and the mean ± 1, ± 2, +3, and +4 standard deviations along the first principal axis.

DATA AND SOFTWARE AVAILABILITY

Computational analysis performed in this paper was performed using custom-written programs in Matlab (Mathworks). The analysis code will be made available upon request.

Supplementary Material

Refer to Web version on PubMed Central for supplementary material.

ACKNOWLEDGEMENTS

We dedicate this paper to the memory of Mike Davidson. We thank Emmanuel Guignet for training on HL60 cell culture and electroporation, Orion Weiner for the HL60 cells expressing actin-YFP, Xuedong Liu for the FG46013 vector for lentivirus production, and Zachary Pincus for developing Celltool. Several of our experiments with microfabricated devices not presented in this manuscript had generated great insights on the mechanics of HL60 migration. These devices were made available through collaborations with Sangmoo Jeong and Yi Cui at Stanford University, and Alex Groisman and Micha Adler at the University of California at San Diego. We thank Lucien Weiss, Thomas Wilson, and W.E. Moerner for help with microscopy, and Alex Mogilner and Kun-Chun Lee for help with the mathematical model. Finally, we would like to thank Kinneret Keren, Cyrus Wilson, Orion Weiner, James Spudich, Jagesh Shah, Harrison Prentice-Mott and members of the Theriot and Ferrell labs for helpful discussions, and Michelle Rengarajan and Lena Koslover for comments on the manuscript. This work was supported by the Howard Hughes Medical Institute (J.A.T.), the National Institutes of Health (GM046383 to J.E.F., GM092804 and EB002503 to D.I and GM074827 to A.Hu.), and by fellowships from the Smith Foundation and Baxter Foundation to T.Y.-C.T, the Helen Hay Whitney Foundation to S.R.C, the Croucher Foundation Joint Universities Summer Teaching Laboratory (JUSTL) program to P-Y.L., Shriners Hospital for Children to F.E., and the BioX Bowes Fellowship and the Alexander S. Onassis Public Benefit Foundation to A.Ha. C. K. C. was supported by the Stanford Cellular and Molecular Biology Training Grant (NIH T32-GM007276) and S. S. L. was supported by the Stanford Medical Scientist Training Program (NIH T32-GM007365). Work in the laboratories of

T.M., J.E.F. and J.A.T. is supported by an NIH program project grant to the Stanford Center for Systems Biology (P50 GM107615).

REFERENCES

Boneschansker L, Yan J, Wong E, Briscoe DM, and Irimia D (2014). Microfluidic platform for the quantitative analysis of leukocyte migration signatures. Nature communications 5, 4787.

Craig R, Smith R, and Kendrick-Jones J (1983). Light-chain phosphorylation controls the conformation of vertebrate non-muscle and smooth muscle myosin molecules. Nature 302, 436–439. [PubMed: 6687627]

Hartman RS, Lau K, Chou W, and Coates TD (1994). The fundamental motor of the human neutrophil is not random: evidence for local non-Markov movement in neutrophils. Biophys J 67, 2535–2545. [PubMed: 7696492]

Hind LE, Vincent WJ, and Huttenlocher A (2016). Leading from the Back: The Role of the Uropod in Neutrophil Polarization and Migration. Developmental cell 38, 161–169. [PubMed: 27459068]

Houk AR, Jilkine A, Mejean CO, Boltyanskiy R, Dufresne ER, Angenent SB, Altschuler SJ, Wu LF, and Weiner OD (2012). Membrane tension maintains cell polarity by confining signals to the leading edge during neutrophil migration. Cell 148, 175–188. [PubMed: 22265410]

Hsiao K-M, Chou S, Shih S-J, Ferrell JE Jr. (1994). Evidence that inactive p42 mitogen-activated protein kinase and inactive Rsk exist as a heterodimer *in vivo*. Proc Natl Acad Sci USA 91:5480–5484 [PubMed: 8202512]

Irimia D (2014). Cell migration in confined environments. Methods in cell biology 121, 141–153. [PubMed: 24560508]

Kimura K, Ito M, Amano M, Chihara K, Fukata Y, Nakafuku M, Yamamori B, Feng J, Nakano T, Okawa K, et al. (1996). Regulation of myosin phosphatase by Rho and Rho-associated kinase (Rho-kinase). Science 273, 245–248. [PubMed: 8662509]

Kitaguchi T, Kawakami K, and Kawahara A (2009). Transcriptional regulation of a myeloid-lineage specific gene lysozyme C during zebrafish myelopoiesis. Mechanisms of development 126, 314–323. [PubMed: 19275935]

Kovacs M, Toth J, Hetenyi C, Malnasi-Csizmadia A, and Sellers JR (2004). Mechanism of blebbistatin inhibition of myosin II. J Biol Chem 279, 35557–35563. [PubMed: 15205456]

Krendel M, Zenke FT, and Bokoch GM (2002). Nucleotide exchange factor GEF-H1 mediates cross-talk between microtubules and the actin cytoskeleton. Nat Cell Biol 4, 294–301. [PubMed: 11912491]

Lam PY, Fischer RS, Shin WD, Waterman CM, and Huttenlocher A (2014). Spinning disk confocal imaging of neutrophil migration in zebrafish. Methods in molecular biology (Clifton, NJ 1124, 219–233.

Lam PY, Yoo SK, Green JM, and Huttenlocher A (2012). The SH2-domain-containing inositol 5-phosphatase (SHIP) limits the motility of neutrophils and their recruitment to wounds in zebrafish. Journal of cell science 125, 4973–4978. [PubMed: 22946052]

Lammermann T, Bader BL, Monkley SJ, Worbs T, Wedlich-Soldner R, Hirsch K, Keller M, Forster R, Critchley DR, Fassler R, et al. (2008). Rapid leukocyte migration by integrin-independent flowing and squeezing. Nature 453, 51–55. [PubMed: 18451854]

Liu YJ, Le Berre M, Lautenschlaeger F, Maiuri P, Callan-Jones A, Heuze M, Takaki T, Voituriez R, and Piel M (2015). Confinement and low adhesion induce fast amoeboid migration of slow mesenchymal cells. Cell 160, 659–672. [PubMed: 25679760]

Maiuri P, Rupprecht JF, Wieser S, Ruprecht V, Benichou O, Carpi N, Coppey M, De Beco S, Gov N, Heisenberg CP, et al. (2015). Actin flows mediate a universal coupling between cell speed and cell persistence. Cell 161, 374–386. [PubMed: 25799384]

Mansour MK, and Levitz SM (2002). Interactions of fungi with phagocytes. Curr Opin Microbiol 5, 359–365. [PubMed: 12160853]

Niederman R, and Pollard TD (1975). Human platelet myosin. II. In vitro assembly and structure of myosin filaments. J Cell Biol 67, 72–92. [PubMed: 240861]

Niggli V (1999). Rho-kinase in human neutrophils: a role in signalling for myosin light chain phosphorylation and cell migration. FEBS Lett 445, 69–72. [PubMed: 10069376]

Niggli V (2003). Microtubule-disruption-induced and chemotactic-peptide-induced migration of human neutrophils: implications for differential sets of signalling pathways. J Cell Sci 116, 813–822. [PubMed: 12571279]

Pearson RB, Jakes R, John M, Kendrick-Jones J, and Kemp BE (1984). Phosphorylation site sequence of smooth muscle myosin light chain (Mr = 20 000). FEBS Lett 168, 108–112. [PubMed: 6546724]

Reymann AC, Boujemaa-Paterski R, Martiel JL, Guerin C, Cao W, Chin HF, De La Cruz EM, Thery M, and Blanchoin L (2012). Actin network architecture can determine myosin motor activity. Science (New York, NY 336, 1310–1314.

Riedl J, Crevenna AH, Kessenbrock K, Yu JH, Neukirchen D, Bista M, Bradke F, Jenne D, Holak TA, Werb Z, et al. (2008). Lifeact: a versatile marker to visualize F-actin. Nat Methods 5, 605–607. [PubMed: 18536722]

Ruprecht V, Wieser S, Callan-Jones A, Smutny M, Morita H, Sako K, Barone V, Ritsch-Marte M, Sixt M, Voituriez R, et al. (2015). Cortical contractility triggers a stochastic switch to fast amoeboid cell motility. Cell 160, 673–685. [PubMed: 25679761]

Safdar A, Chaturvedi V, Cross EW, Park S, Bernard EM, Armstrong D, and Perlin DS (2001). Prospective study of Candida species in patients at a comprehensive cancer center. Antimicrob Agents Chemother 45, 2129–2133. [PubMed: 11408236]

Sakamoto T, Limouze J, Combs CA, Straight AF, and Sellers JR (2005). Blebbistatin, a myosin II inhibitor, is photoinactivated by blue light. Biochemistry 44, 584–588. [PubMed: 15641783]

Segal AW (2005). How neutrophils kill microbes. Annu Rev Immunol 23, 197–223. [PubMed: 15771570]

Senda N, Tamura H, Shibata N, Yoshitake J, Konko K, and Tanaka K (1975). The mechanism of the movement of leucocytes. Experimental cell research 91, 393–407. [PubMed: 165089]

Smith RC, Cande WZ, Craig R, Tooth PJ, Scholey JM, and Kendrick-Jones J (1983). Regulation of myosin filament assembly by light-chain phosphorylation. Philos Trans R Soc Lond B Biol Sci 302, 73–82. [PubMed: 6137010]

Spellberg BJ, Collins M, French SW, Edwards JE Jr., Fu Y, and Ibrahim AS (2005). A phagocytic cell line markedly improves survival of infected neutropenic mice. J Leukoc Biol 78, 338–344. [PubMed: 15857941]

Svitkina TM, Verkhovsky AB, McQuade KM, and Borisy GG (1997). Analysis of the actin-myosin II system in fish epidermal keratocytes: mechanism of cell body translocation. The Journal of cell biology 139, 397–415. [PubMed: 9334344]

Uchida KS, Kitanishi-Yumura T, and Yumura S (2003). Myosin II contributes to the posterior contraction and the anterior extension during the retraction phase in migrating Dictyostelium cells. J Cell Sci 116, 51–60. [PubMed: 12456715]

Wang F (2009). The signaling mechanisms underlying cell polarity and chemotaxis. Cold Spring Harbor perspectives in biology 1, a002980. [PubMed: 20066099]

Wang F, Herzmark P, Weiner OD, Srinivasan S, Servant G, and Bourne HR (2002). Lipid products of PI(3)Ks maintain persistent cell polarity and directed motility in neutrophils. Nat Cell Biol 4, 513–518. [PubMed: 12080345]

Wang Y, Ku CJ, Zhang ER, Artyukhin AB, Weiner OD, Wu LF, and Altschuler SJ (2013). Identifying network motifs that buffer front-to-back signaling in polarized neutrophils. Cell Rep 3, 1607–1616. [PubMed: 23665220]

Weiner OD, Neilsen PO, Prestwich GD, Kirschner MW, Cantley LC, and Bourne HR (2002). A PtdInsP(3)- and Rho GTPase-mediated positive feedback loop regulates neutrophil polarity. Nat Cell Biol 4, 509–513. [PubMed: 12080346]

Weiner OD, Marganski W,A, Wu LF, Altschuler SJ, Kirschner MW (2007). An actin-based wave generator organizes cell motility. PLoS Biol., 5, p. e221 [PubMed: 17696648]

Wilson CA, Tsuchida MA, Allen GM, Barnhart EL, Applegate KT, Yam PT, Ji L, Keren K, Danuser G, and Theriot JA (2010). Myosin II contributes to cell-scale actin network treadmilling through network disassembly. Nature 465, 373–377. [PubMed: 20485438]

Wong K, Pertz O, Hahn K, and Bourne H (2006). Neutrophil polarization: spatiotemporal dynamics of RhoA activity support a self-organizing mechanism. Proceedings of the National Academy of Sciences of the United States of America 103, 3639–3644. [PubMed: 16537448]

Wong K, Van Keymeulen A, and Bourne HR (2007). PDZRhoGEF and myosin II localize RhoA activity to the back of polarizing neutrophil-like cells. The Journal of cell biology 179, 1141–1148. [PubMed: 18086913]

Xu J, Wang F, Van Keymeulen A, Herzmark P, Straight A, Kelly K, Takuwa Y, Sugimoto N, Mitchison T, and Bourne HR (2003). Divergent signals and cytoskeletal assemblies regulate self-organizing polarity in neutrophils. Cell 114, 201–214. [PubMed: 12887922]

Yang HW, Collins SR, and Meyer T (2015). Locally excitable Cdc42 signals steer cells during chemotaxis. Nature cell biology 18, 191–201. [PubMed: 26689677]

Yoo SK, Deng Q, Cavnar PJ, Wu YI, Hahn KM, and Huttenlocher A (2010). Differential regulation of protrusion and polarity by PI3K during neutrophil motility in live zebrafish. Developmental cell 18, 226–236. [PubMed: 20159593]

Yoo SK, Lam PY, Eichelberg MR, Zasadil L, Bement WM, and Huttenlocher A (2012). The role of microtubules in neutrophil polarity and migration in live zebrafish. Journal of cell science 125, 5702–5710. [PubMed: 22992461]

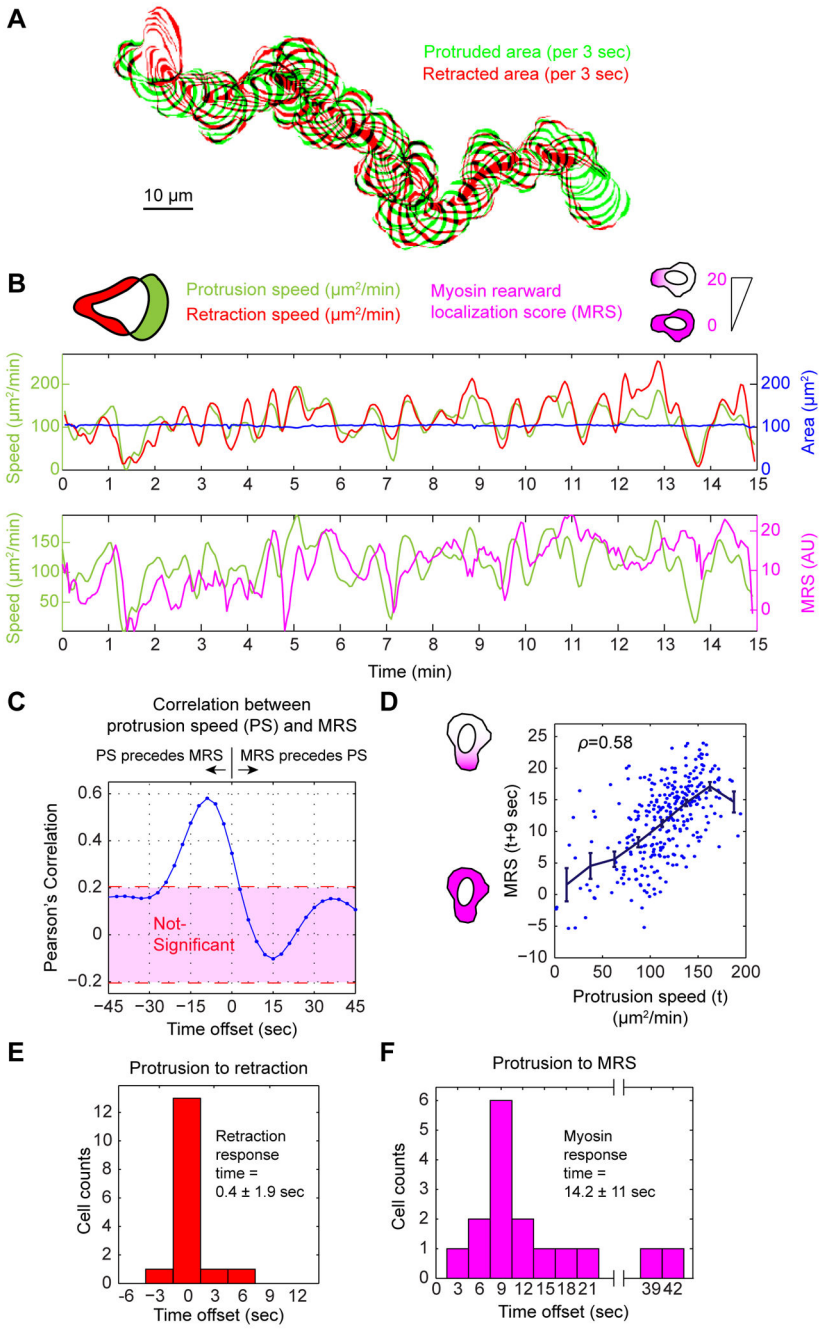

Figure 1. Protrusion and retraction are closely coupled in migrating HL60 cells, while myosin accumulation lags.

(A) A 15 min trace of a migrating HL60 cell. Newly protruded area (green) and newly retracted area (red) were calculated every 3 sec. Individual cell outlines are shown at 9 sec intervals.

(B) A 15 min trace of the protrusion speed (green), retraction speed (red), and myosin rearward localization score (MRS) (magenta), for the cell shown in (A). Total cell area over the same time frame is shown in blue.

(C) Cross-correlation between the protrusion speed and MRS, for the same cell. A negative offset means the protrusion precedes the MRS. The magenta shaded region represents a correlation that is below 95% confidence interval.

(D) A scatter plot comparing protrusion speed and MRS 9 sec later over the course of a single 15 min movie. We binned the data with a width of 25 μm^2/min. The dark blue line is mean ± SEM. The Pearson's correlation score (p) is 0.58, corresponding to the peak value in (C).

(E-F) Summary of the temporal offset between protrusion and retraction (E), and between protrusion and MRS (F) in 16 movies from 12 cells. In all cases, the change of protrusion speed precedes the change of the MRS.

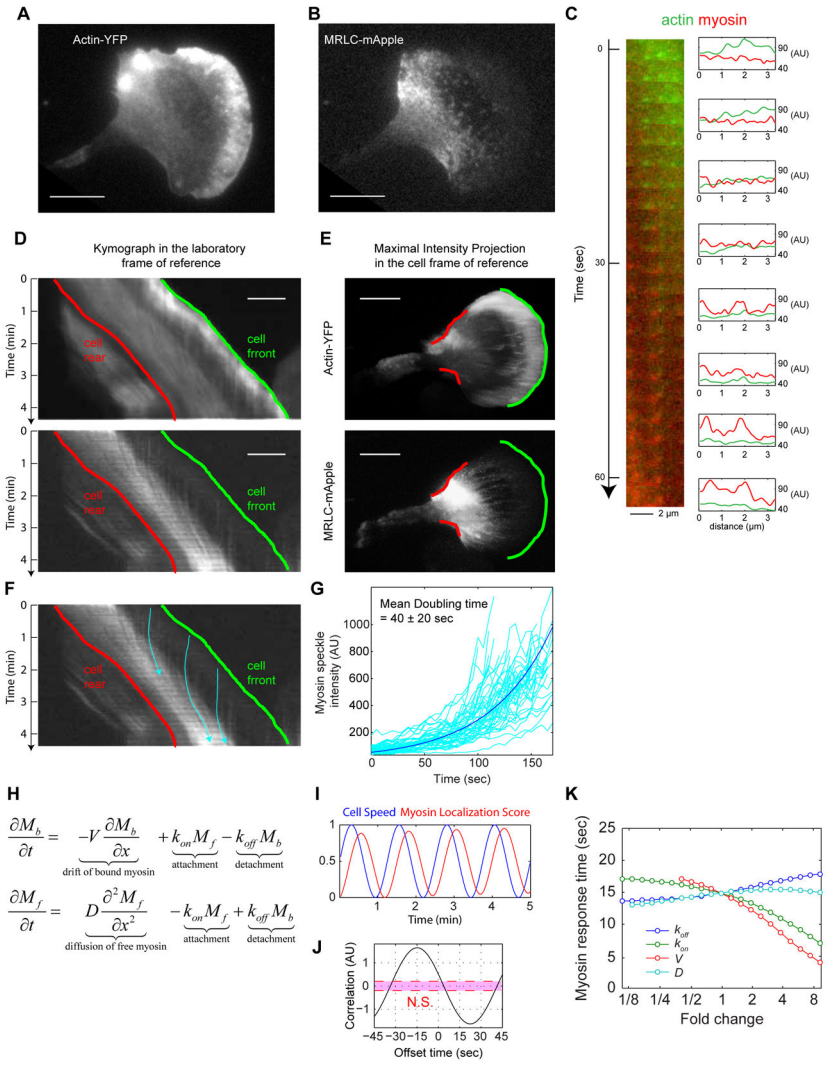

Figure 2. MRLC retrograde flow and membrane retraction facilitate the rapid coupling between protrusion and myosin II redistribution.

(A-B) TIRF images of (A) actin-YFP and (B) MRLC-mApple, coexpressed in an HL60 cell. The images are representative of 20 different cells. Scale bars in (A,B,D,E) are 10 μm.

(C) A magnified image sequence showing the transition from actin puncta to myosin puncta. The image at the left is a montage of the same region in the laboratory frame of reference over a 63 sec period. The diagrams at the right show the fluorescence intensity of line scans from the corresponding image at the left. In the lab frame of reference, the actin and myosin puncta at the front of the cell remain static relative to the substrate.

(D) Kymographs of actin-YFP (top) and MRLC-mApple (bottom) in the lab frame of reference. Each row of the kymograph is obtained by a 2.6 μm-wide line scan through the middle of the cell along the migration direction. Cell is migrating towards the right. The green line corresponds to the green leading edge in (E) and the red line corresponds to the red retracting edge in (E).

(E) Maximal intensity projection of actin-YFP (top) and MRLC-mApple (bottom) in the cell frame of reference, showing the direction of actin (top) and MRLC (bottom) retrograde flow.

The image integrated the fluorescent signals over a 96 sec period. Green color marks the leading edge and red color marks the retracting edge. Image contrast in A,B,E was adjusted to emphasize the actin and myosin puncta.

(F) The trajectories of three individual myosin puncta (blue).

(G) The rate of increase of fluorescence intensity from 67 MRLC puncta in a single cell was measured to estimate the binding rate of myosin to F-actin (see Methods). The average apparent doubling time for myosin accumulation was 40 ± 20 sec.

(H) A partial differential equation model in one dimension with only two variables: M_b is the bound myosin and M_f is the cytoplasmic (free) myosin. The four parameters are V (velocity of the retrograde flow), D (diffusion coefficient of the cytoplasmic myosin), k_{on} (attachment rate of myosin to F-actin), and k_{off} (detachment rate of bound myosin from F-actin).

(I) The response of myosin localization score to a simulated oscillatory speed with a period of 1.25 min.

(J) The cross-correlation analysis between the cell speed and the myosin localization score generated a temporal offset of 15 sec.

(K) A sensitivity analysis of the response time of myosin when each of the four parameters are tuned up or down 9-fold.

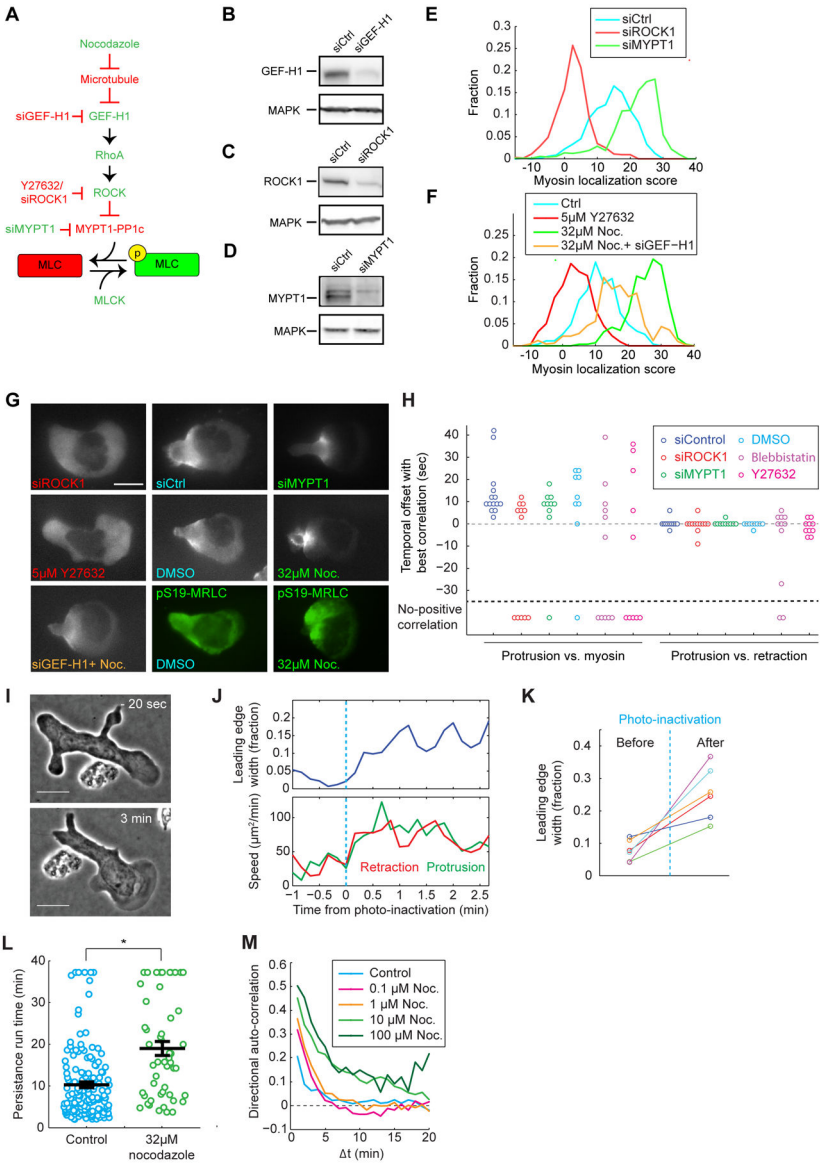

Figure 3. Intracellular myosin distribution depends on phosphorylation of myosin regulatory light chain. Myosin contractility is dispensable for front-rear coupling, but affects leading edge dynamics.

(A) A signaling cascade regulating MRLC phosphorylation. A protein or perturbation that increases or decreases MRLC phosphorylation are colored green or red, respectively.

(B-D) Western blots of HL60 cell lysates on GEF-H1 (B), ROCK1(C), MYPT1(D) and MAPK(B-D), showing the effective knockdown of GEF-H1(B), ROCK1(C), and MYPT1(D) by siRNA. Each blot has been repeated 2 or 3 times.

(E-F) Histogram of myosin rearward localization score under different conditions. Sample sizes in the format of (number of images, number of cells): siCtrl (726,66), siROCK1 (649, 59), siMYPT1 (737,67), control (275,55), Y27632 (220,44), nocodazole (285,57), nocodazole + siGEF-H1 (506,46)

(G) Representative snapshots of MRLC-mApple fluorescent images of HL60 cells under different treatments. The two images in green are HL60 cells immunostained with antibody targeting pS19-MRLC. Scale bar is 10 μm.

(H) Summary of the temporal offset between protrusion and retraction (right), and between protrusion and myosin rearward localization score (left). Sample sizes in the format of (number of movies, number of cells): siControl (14,10), siROCK1 (12,12), siMYPT1 (10, 7), DMSO control (9,6), 10μM blebbistatin (11,11), 10uM Y27632 (10,10)

(I) Snapshots of a blebbistatin-treated cell 20 sec before and 3 min after photo-inactivation. Scale bar is 10 μm.

(J) Leading edge, protrusion, and retraction speed before and after blebbistatin photo-inactivation for the cell shown in (I). In (J-K), leading edge width is calculated as the fraction of cell circumference that is actively protruding. Protrusion and retraction speed are defined as in Figure 1B.

(K) Change of leading edge width from 6 cells in 3 experiments before and after blebbistatin photo-inactivation. The representative cell shown in (I) and (J) corresponds to the data points in green.

(L) Persistence run time for control and nocodazole-treated cells. Each circle represents the average persistence run time for one single cell over an observation time of 40 min. The black lines represent the average, and the average ± standard error of the mean. Control (152 cells from 2 experiments) and nocodazole-treated (52 cells from 2 experiments) values are significantly different at $p < 0.005$ by Student's t-test (**).

(M) The directional auto-correlation (see Methods) of nocodazole-treated cells.

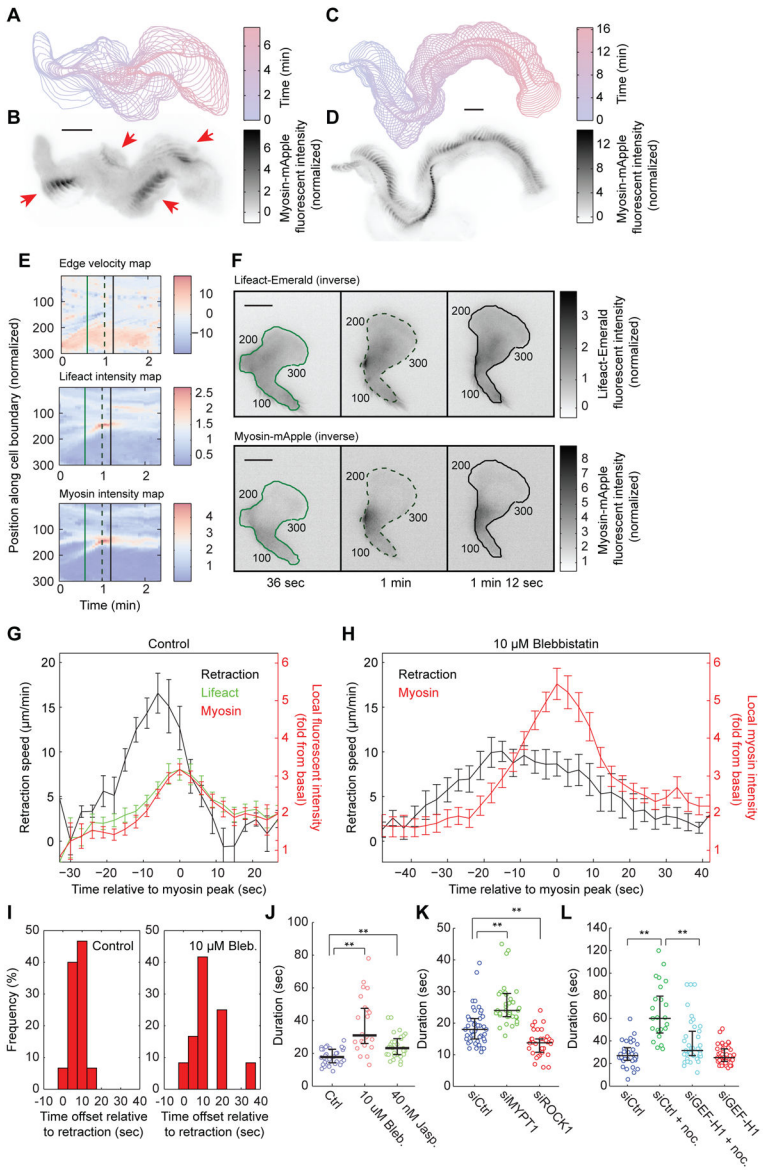

Figure 4. Myosin contraction mediates rapid flashes at the cell rear.

(A,C) Contours of a migrating HL60 cell over (A) 400 sec and (C) 970 sec, with 10 sec intervals.

(B,D) Maximal intensity projection of inverse fluorescent images of MRLC-mApple from migrating cells in (A) and (C). The fluorescence intensity was normalized to the average intensity of the whole cell. (B) The red arrows highlight the spatial discontinuity of each myosin flash. The flashes are typically located at the outside of the turning trajectory. Scale bars in (A-D, F) are 10 μm.

(E) Local edge velocity, local Lifeact-mEmerald intensity, and local MRLC-mApple intensity along the boundary of the cell over 138 sec. In the edge velocity map, a positive velocity represents local protrusion and a negative velocity represents local retraction, with the unit of μm/min. In the local F-actin intensity map and the local myosin intensity map, the fluorescence intensity is normalized to the average of the cell.

(F) Snapshots of inverse fluorescent images of Lifeact-mEmerald and MRLC-mApple during a flash. All the fluorescent images are inverted. The three time points correspond to the three vertical lines in (E). The number index along the cell contour corresponds to the number along the vertical axis in the three heatmaps in (E).
(G-H) Average dynamics of the myosin flashes from (G) control cells (16 flashes from 3 cells) and (H) blebbistatin-treated cells (14 flashes from 4 cells). Error bars are s.e.m.
(I) Distribution of temporal offset between local myosin concentration and local retraction velocity in non-treated (15 flashes from 3 cells) and blebbistatin-treated (12 flashes from 4 cells) cells. A positive value means myosin dynamics lags behind retraction velocity.
(J-L) Statistics of the duration of the myosin flashes under different conditions. Each open circle represents the average duration of a single cell observed for more than 10 min. Cell numbers: (J) Control (30), blebbistatin (24), jasplakinolide (30). (K) siCtrl (46), siMYPT1 (36), siROCK1 (34). (L) siCtrl (33), siCtrl + nocodazole (25), siGEF-H1 + nocodazole (42), siGEF-H1 (42). ** $p < 0.005$ (Student's t-test).

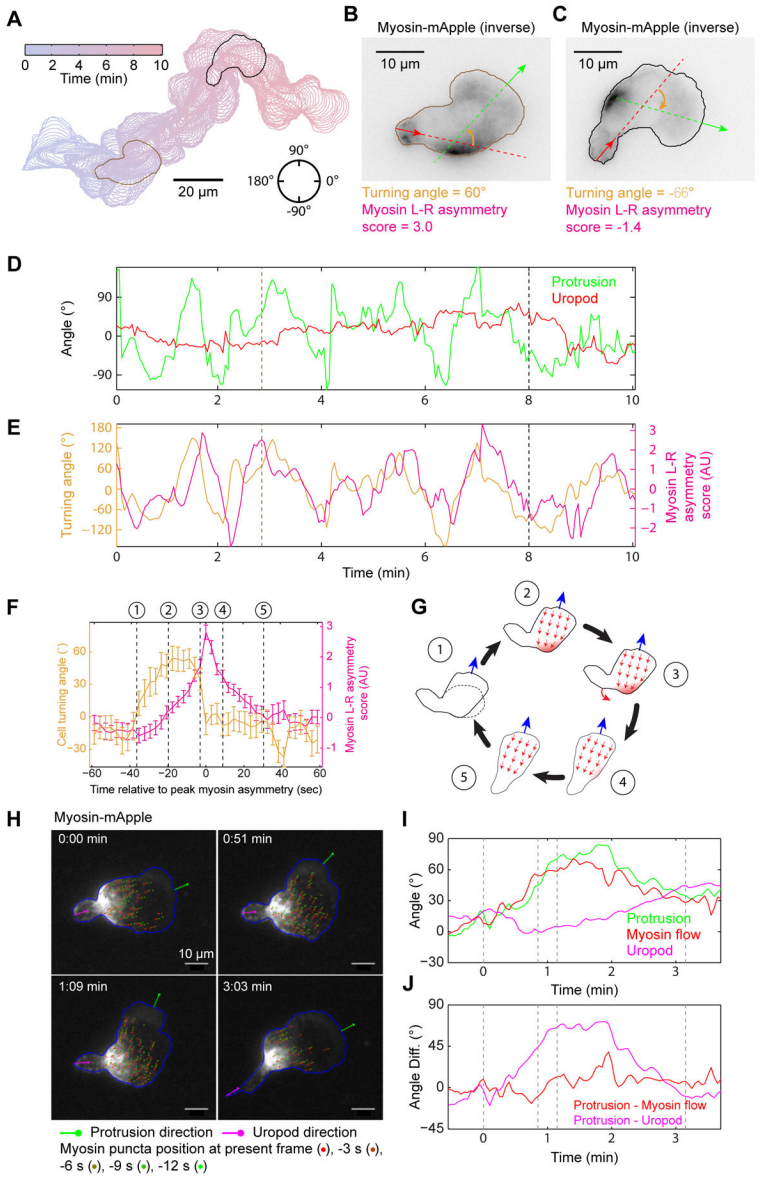

Figure 5. Asymmetric myosin localization follows directional change of the protrusion to facilitate efficient turning.

(A) A 10-min trajectory of a frequently turning HL60 cell, with 3 sec intervals.

(B-C) Snapshots of inverse fluorescent images of MRLC-mApple at (B) 2 min 51 sec and (C) 8 min as examples for cells turning left (B) or right (C). Green arrows represent the direction of protrusion, defined as the normal vector from the point at the leading edge with maximal protrusion speed. Red arrows represent the normal direction from the tip of the uropod. The turning angle of the cell is defined as the difference of the green and red arrows, shown in orange. In both cases, myosin localizes to the outside of the turn.

(D) The direction of protrusion (green) and uropod (red) throughout the 10 min trajectory. The direction is defined in the circle in (A), with 0° pointing to the right and the angle increases counter-clockwise to 180°, and decreases clockwise to −180°.

(E) Turning angle (orange) and myosin left-right asymmetry score (red) throughout the 10 min trajectory. The myosin asymmetry appears to lag behind the turning of the protrusion. (D-E) The brown and black dashed lines correspond to the image shown in (B) and (C), respectively.

(F) Summary of the average turning dynamics and the corresponding myosin left-right asymmetry score from 46 turning events in 6 different cells. The signs of myosin asymmetry score and turning angle from a right turn are inversed to allow averaging with left turns. At each turn, the peak of myosin asymmetry is defined as time 0. The turning dynamics and myosin asymmetry score from −60 sec to 60 sec in all 46 turns are averaged. Error bars are s.e.m..

(G) Cartoon illustration of the temporal sequence during a turn. The numbers 1 to 5 correspond to the numbers 1 to 5 along the temporal axis in (F).

(H) TIRF images of myosin flow in a turning HL60 cell. Green lines are the directions of protrusion. Magenta lines are the directions of the uropod. Blue lines outline the cell contours. Movement of individual myosin puncta in the cell frame of reference were shown for 5 consecutive frames and marked with different.

(I-J) Myosin flow direction closely follows the protrusion direction, while the uropod lags behind during cell turning. Panel (I) shows the direction of protrusion (green), myosin flow (red) and uropod (magenta) in the lab frame of reference. Panel (J) shows the differences between protrusion direction and myosin flow (red) and between protrusion and uropod direction (magenta)

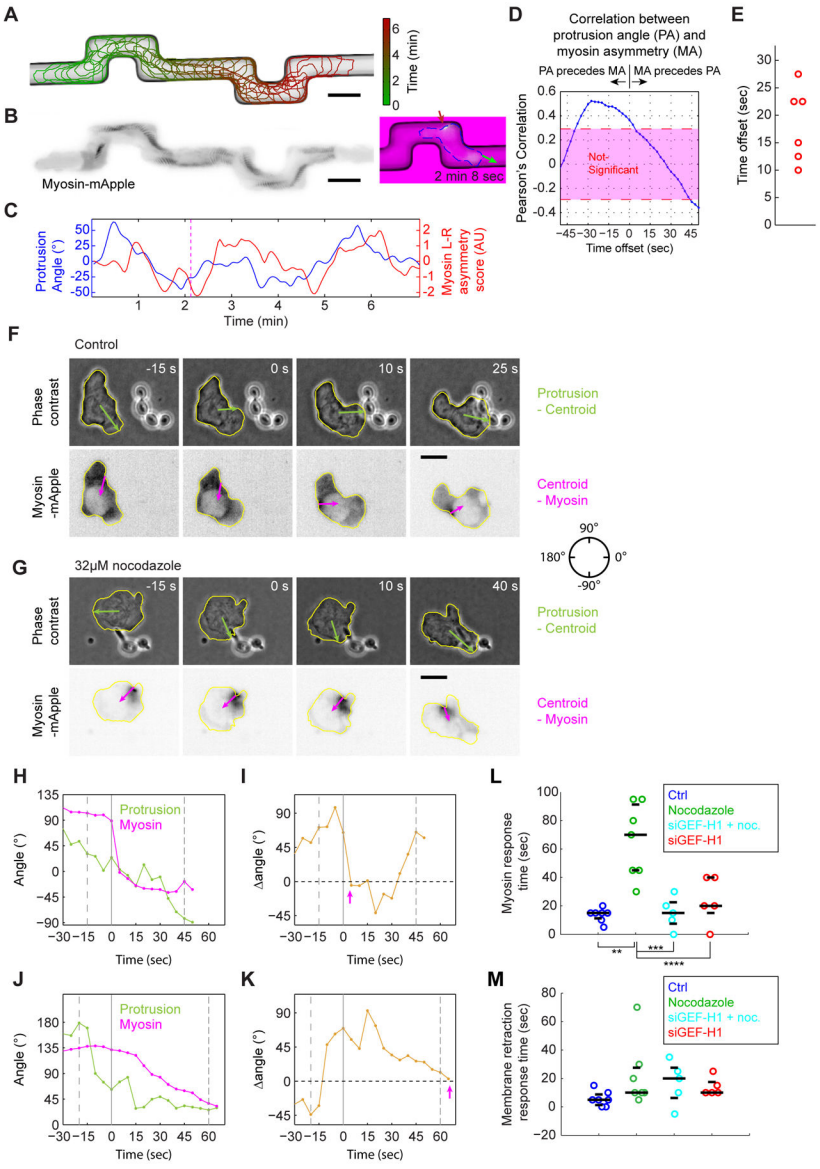

Figure 6. Rapid myosin dynamics is preserved in HL60 cells forced to turn mechanically, and facilitates quick re-orientation of the rear during chemotaxis

(A) A 6.7 min trajectory of a HL60 cell migrating within a microfluidic channel, with 12.5 sec intervals. Scale bars in (A,B,F,G) are 10 μm.

(B) A maximal intensity projection of the MRLC-mApple fluorescent images. The colored image at the right of the maximal intensity projection is a snapshot when the cell is turning within the channel. Green arrow indicates the protrusion direction, while the red arrow highlights the myosin flash.

(C) The dynamics of protrusion angle (blue) versus myosin left-right asymmetry score (red) reveal the correlation between the two parameters with some temporal offset.

(D) Cross-correlation analysis between the protrusion angle and the myosin left-right asymmetry shown in (C) reveals maximal correlation at an offset of 27.5 sec.

(E) Summary of the temporal offset between protrusion angle and myosin left-right asymmetry in 6 distinct movies from 3 cells migrating in the microfluidic channel. Each movie contains at least 3 90° turns.

(F-G) Snapshots of phase contrast images and inverted MRLC-mApple fluorescent images from a (F) control or (G) nocodazole-treated HL60 cell migrating towards a *C. albicans* cell. The green arrows are the directions from the cell centroid to the point with fastest protrusion velocity. The magenta arrows are the direction from the point with maximal myosin intensity to the cell centroid.

(H,J) The temporal dynamics of protrusion direction and myosin contraction direction as the (H) control and (J) nocodazole-treated cell approaches the *C. albicans* cell.

(I,K) The angular difference between the protrusion and myosin contraction direction as the (I) control and (K) nocodazole-treated cell approaches the fungal cell. The pink arrows represent the recorded myosin response time in (L).

(H-K) The first dashed line represents the initiation of the turning event. The second solid line represents the time when the protrusion direction aligns with the *C. albicans* cell. The last dashed line represents the completion of phagocytosis.

(L) The response time of myosin localization after the protrusion aligns with the *Candida* cell under different conditions. Response time of nocodazole-treated cells is significantly different from all other samples with $p < 0.05$ (*) or $p < 0.005$ (**) by Student's t-test.

(M) The response time of membrane retraction after the protrusion aligns with the *Candida* cell under different conditions.

(L.M) The three black lines are the 25th, 50th, and 75th percentile of the data. Sample sizes in the format of (number of cells, number of experiments): Control (7,2), nocodazole (7, 4), siGEF-H1 + nocodazole (5,2), siGEF-H1 (5,2).

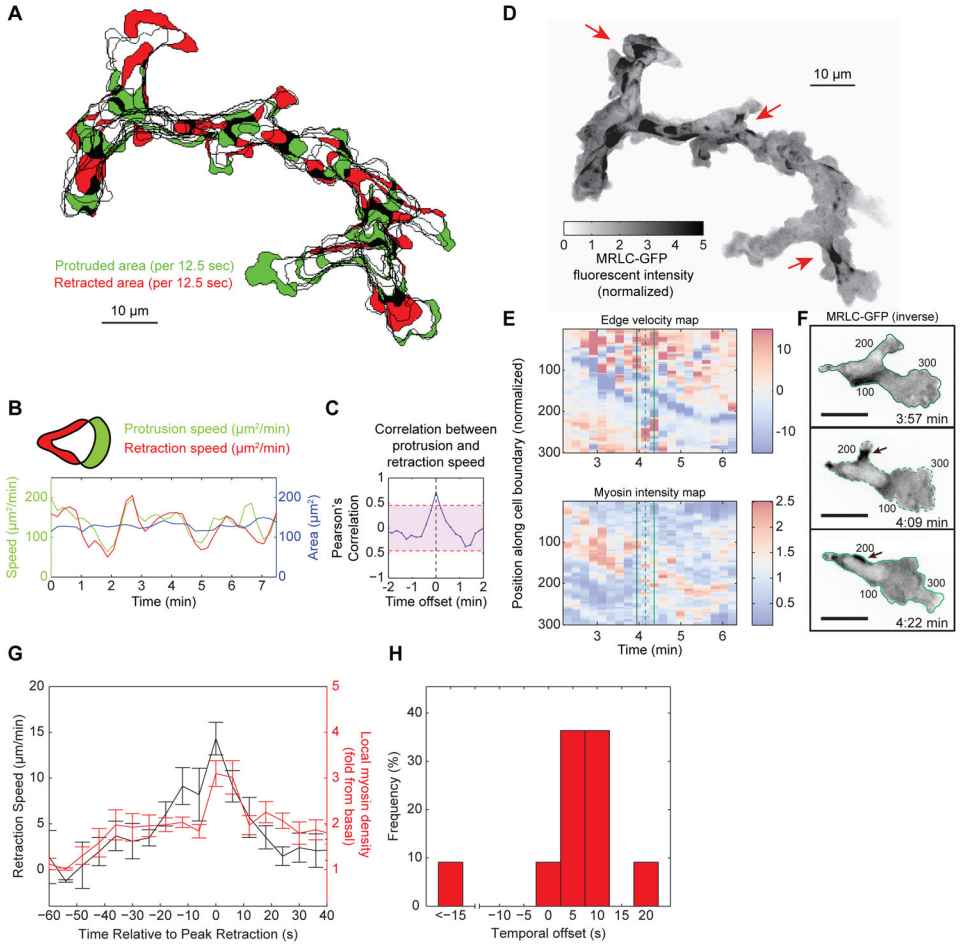

Figure 7. Efficient front-rear coupling and dynamic myosin localization in migrating neutrophils *in vivo*

(A) A 7 min trajectory of a migrating neutrophil in 3-day old zebrafish larvae with 12.5 sec intervals. Newly protruded area (green) and newly retracted area (red) were calculated every 12.5 sec. Only one third of the time points were colored with green or red for ease of visualization.

(B) A 7 min trace of the protrusion speed (green), retraction speed (red) for the cell shown in (A). Total cell area over the same time frame is shown in blue.

(C) Cross-correlation between the protrusion speed and the retraction speed for the same cell, showing maximal correlation at zero temporal offset. The magenta shaded region represents a correlation that is below 95% confidence interval.

(D) Maximal intensity projection of inverse fluorescent images of MRLC2-EGFP from migrating cells in (A). The red arrows highlight the spatial discontinuity of each myosin flash. Scale bars in (A,D) are 10 μm.

(E) Local edge velocity and local MRLC2-EGFP intensity along the cell boundary. In the edge velocity map, a positive velocity represents local protrusion and a negative velocity represents local retraction, with the unit of μm/min. In the local myosin intensity map, the fluorescence intensity is normalized to the lowest 10% of the cell.

(F) Snapshots of MRLC2-EGFP fluorescent images during a flash. All the fluorescent images are inverted. The three time points correspond to the three vertical lines in (E). The number index along the cell contour corresponds to the number along the vertical axis in the heatmaps in (E). Scale bars are 10 μm.

(G) Average dynamics of local edge retraction velocity and local myosin concentration. Error bars are s.e.m.

(H) Distribution of temporal offset between local myosin concentration and local retraction velocity. A positive value means myosin dynamics lags behind retraction velocity.